

9

23

24

26

27

28

29

30



# Direct Estimation of Wildfire Emissions at High Latitudes from Combined Polar Orbiter FRP and Sentinel-5P CO Data

- 3 William M. Maslanka<sup>1,2</sup>, Martin J. Wooster<sup>1,2,3</sup>, Zixia Liu<sup>1,2</sup>, Jiangping He<sup>1,2</sup>
- 4 Department of Geography, King's College London, London, WC2R 2ND, UK
- 5 <sup>2</sup>National Centre for Earth Observation (NCEO), London, UK
- 6 <sup>3</sup>Leverhulme Centre for Wildfires, Environment and Society, London, UK
- 8 Correspondence to: William M. Maslanka (william.maslanka@kcl.ac.uk)

10 significance under rapid anthropogenic climate change-induced warming. Current fire emission inventories are mostly 'bottom-up' in nature; combining, or relying on linear regressions between, satellite remote sensing data and process-based 11 model outputs. However, these methods rely on uncertainties surrounding fuel load and combustion completeness. Here, we 12 adapt the 'top-down' Fire Radiative Energy Emission (FREM) approach for HL fires (HLFREM), linking Fire Radiative 13 14 Energy (FRE) directly to emissions via coefficients derived solely from satellite observations. We derive biome-specific emission coefficients by combining Fire Radiative Power (FRP) from GFAS v1.4 with TROPOMI Total Column Carbon 15 Monoxide plume observations, for the HL's four most fire-prone biomes; Deciduous and Evergreen Needleleaf Forests, 16 Grasslands, and Shrublands. By applying these coefficients to daily GFAS v1.2 FRE totals (2003-2024), we estimate CO and 17 total carbon emissions across the HL using HLFREM. HLFREM-derived CO emissions generally agree with other widely 18 19 used inventories (GFAS v1.2, FEERv1.0-GFASv1.2, and GFEDv4.1s) in forested biomes, with annual average differences of 20 -32% to -43% for Deciduous Needleleaf Forests, and -28% to -43% for Evergreen Needleleaf forests. For Shrublands and Grassland biomes, HLFREM estimates are 31-43% and 61-80% lower respectively. Total carbon emissions, using Emission 21 22 Factors, were found to show consistent patterns with CO across all biomes. Our results represent the first HL fire emissions

Abstract. High Latitude (HL) landscape fires are an important source of greenhouse gases and aerosols, with growing

# 25 1. Introduction

release.

Landscape fire is Earth's largest natural disturbance agent, burning, according to the latest satellite-derived datasets, an average of approximately 5.5% of Earth's land surface annually (Chen et al., 2023). These landscape fires greatly affect ecology, land carbon stores, atmospheric composition, air quality, and human health. The true magnitude of these effects may even be higher than currently estimated, due to satellite-based burned area mapping often missing many of the highly-numerous smaller burns that together make up a significant fraction of total global burned area (Ramo et al., 2021), even when adjusted for some of this low bias (Chen et al., 2023).

dataset based only on satellite data of a major carbon containing gas (CO) emitted by fires and the rate of fire radiative energy

for some of this low bias (Chen et al., 2023).

Satellite data indicates that vegetation fires are extensive across every vegetated continent apart from Antarctica, including even High Latitude (HL, ≥ 60°N) areas (Jones et al., 2022) up to 75°N (Masrur et al., 2018). Such HL burns include so-called 'Arctic-fires' (i.e. fires taking place at latitudes above 66°N) which are of increasing interest, in part because evidence suggests an increase in both their frequency and magnitude; potentially driven by the rapid warming of Earth's climate occurring in





more northerly regions (McCarty et al., 2021). These Arctic-fires, for example those in Siberia in 2020 and 2021 (Kharuk et al., 2021; Liu et al., 2022) can be seen as an extension of the wider northern (i.e. Boreal) regions' fire activity (McCarty et al., 2021), which is itself apparently increasing (Masrur et al., 2018). This is most commonly attributed to lengthening of the 'fire season', the period of the year when vegetation, litter and/or organic soils are sufficiently warm and dry for significant landscape fires to ignite and spread.

Frequent lightning, and the extensive uninterrupted fuel (primarily forest) cover, promotes fire in many HL areas; with certain tree species having evolved to include fire as part of their reproductive cycle (Hodges et al., 2021; Hutto, 2008). Such adaptations and their regionally varying occurrence in HL regions are apparently behind many of the spatial differences seen in certain remotely sensed fire signatures (Rogers et al., 2015; Wooster and Zhang, 2004). Because many of the forests of the HL regions ultimately require fire to thrive, wildfires are often left to burn without intervention if they pose little-to-no threat to humans or property. However, there is a concern that the massive stores of ground carbon contained in the underlying peat and organic soils of northern regions, some of which have remained frozen for millennia, may also be becoming more accessible to fire (Davidson and Janssens, 2006; Turetsky et al., 2002). Burning of these carbon stores results in net greenhouse gases (GHGs) emissions that are unreplaced by photosynthetic carbon reassimilation (i.e. vegetation regrowth) on the decades-to-century time-scales typical of forest recovery (Friedlingstein et al., 2021). Quantifying HL fire activity and any trends in its nature is therefore valuable for understanding fires contribution to net atmospheric greenhouse gas concentrations (Mekonnen et al., 2022), as well as for issues such as air quality (Warneke et al., 2023).

Calculating the amount of land carbon (i.e. live vegetation, litter and, organic soil) consumed by fire, including in HL fires, as well as emissions of Carbon Monoxide (CO) and other GHGs, reactive gases, and aerosols, typically involves a so-called "bottom-up" calculation (Crutzen and Andreae, 1990), with the most modern implementations combining modelling and satellite-derived datasets (Ichoku and Ellison, 2014; Kaiser et al., 2012; van der Werf et al., 2010, 2017). The most common implementation, the Global Fire Emission Database (GFED, (Randerson et al., 2017)), is driven by satellite-derived measures of burned area, but is still classed as an 'indirect' approach since it relies heavily on mathematical models and/or in-situ assessments for the fuel load and combustion completeness parameters that remain subject to significant uncertainty at any particular location (Reid et al., 2009). An alternative satellite-based 'direct' approach relies on Fire Radiative Power (FRP) measures rather than burned area, with FRP representing the radiant energy released per unit time by the combustion process. These FRP data can be time-integrated to estimate the Fire Radiative Energy (FRE) released by the burn, which then links to total fuel consumption (Roberts et al., 2005; Wooster et al., 2005, 2015). FRP-based approaches avoid the need for assumed or modelled fuel load and combustion completeness terms (Kasischke and Penner, 2004), but are not always fully independent of the burned area-based methods since the necessary 'FRP-to-fuel consumption' conversion coefficients are themselves often derived from correlations and regressions made between FRE datasets and the outputs of the more indirect burned area-based approach; such as with the Global Fire Assimilation System (GFAS, (Kaiser et al., 2012)). Alternatively, such conversion coefficients have been based on limited numbers of direct comparisons between FRE and fuel consumption, but in mostly small-scale or laboratory burns which may not accurately represent the dynamics of real landscape scale fires, nor the full



72

73

74

75 76

77

78

79

80

81

82

83

84 85

86

87

88

89 90

91

92

93

94

95

96



characteristics of the FRP measurements made from Earth orbit (Freeborn et al., 2008; Nguyen and Wooster, 2020; Wooster et al., 2005).

More recently, even more direct "top-down" FRP-based emissions assessment methodologies have emerged; now relating smoke emissions directly to the observed FRP of landscape fires. Their uniqueness is that, in order to reduce the aforementioned issues and embedded assumptions that arise when using satellite-derived FRE totals with 'FRP-to-fuel consumption' conversion coefficients, these new approaches use direct satellite-based measurements of fire emissions and FRP, via a set of 'matchup fires', to generate a set of landscape-fire 'emissions coefficients' that can be used to generate smoke emissions estimates directly from all other FRP observations of the area. One of the most recent such approaches, termed the Fire Radiative Energy Emissions (FREM) method (Mota and Wooster, 2018; Nguyen and Wooster, 2020), derives these emissions coefficients directly from geostationary satellite FRE estimates and matching smoke plume Earth observation data (Fisher et al., 2020; Mota and Wooster, 2018; Nguyen and Wooster, 2020). Emissions coefficients derived in this way are appropriate to real landscape fires of all sizes, minimally reliant on any assumptions, and appropriate to apply to further satellite FRE data to convert them into smoke emissions estimates (Nguyen et al., 2023). Thus far, the FREM approach has relied on geostationary satellites to provide the high imaging frequency FRP data with which to accurately estimate FRE via temporal integration. Observations made by equatorial orbit geostationary satellites are, however, of mostly poor quality at high latitudes. However, whilst FRP-to-FRE calculations based on polar orbiting satellite data can be challenging at lower latitude fires due to the limited temporal sampling of FRP provided (Mota and Wooster, 2018), at higher latitudes orbital convergence generally provides far more polar-orbiting based estimates of FRP per day (Fig. 1).

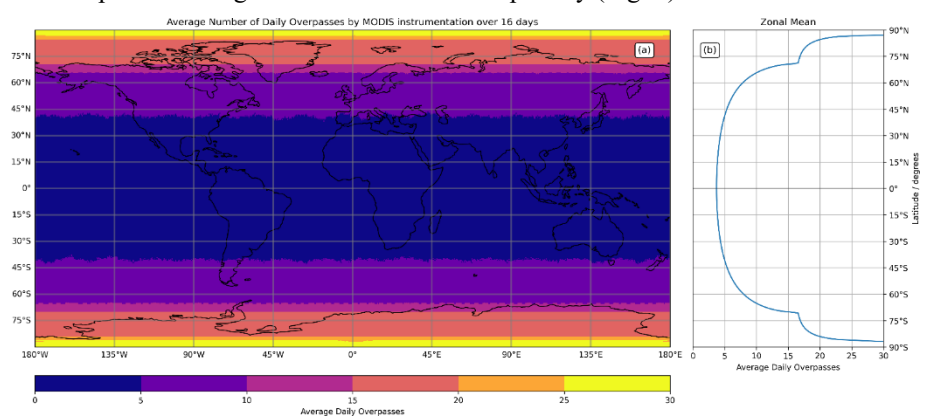


Figure 1: (a) Mean number of daily overpasses at any Earth location made by MODIS on AQUA and TERRA, and (b) zonal mean number of daily overpasses. Daily averages based on 16 days of data taken between 11/08/24 00:00 UTC and 27/08/24 00:00 UTC, gridded to a regular 0.5° x 0.5° grid. At latitudes where HL fires occur (60° - 75°N), there is a latitudinal observation frequency dependence that provides on average between 8 and 18 daily satellite observations from these two systems alone. Each cloud-free observation provides an FRP measure, and which can be used to estimate FRE via temporal integration.

Here we aim to take advantage of the higher latitude, higher temporal resolution sampling of FRP to develop a HL version of the current FREM approach of Nguyen et al., (2023); generating for the first time a dataset of HL fire carbon and trace gas emissions completely independent of satellite-derived burned area measures and/or of the FRP-to-fuel consumption conversion





coefficients influenced by them. These conversion coefficients are also not derived from small-scale experiments, but from Earth observation data of the landscape fires themselves. We compare our fire emissions assessments to those of existing state-of-the-art burned area and FRP based approaches, and assess the characteristics and benefits of our approach with respect to these alternatives. In Sect. 2, we provide the background to the FREM approach. In Sect. 3, we describe its adaptation for HL fires (hereby referring to the method as HLFREM) and using satellite derived polar orbiter FRP data and plume-integrated Total Column Carbon Monoxide (TCCO) observations we derive biome (b) specific emission coefficients for Carbon Monoxide ( $EC_{CO}^b$ ) and Carbon ( $EC_{CO}^b$ ), as well as total CO and carbon emissions via their use with FRP time-series data. In Sect. 4, we calculate the total CO and Carbon emissions, using  $EC_{CO}^b$  and  $EC_{CO}^b$ , and compare them to the fire emissions estimates present in other widely used inventories, before closing with a Summary and Conclusion in Sect. 5.

# 2. FREM Background

As detailed in the review of Wooster et al., (2021), both geostationary satellites (Wooster et al., 2015; Xu et al., 2010, 2017, 2021) and polar-orbiting satellites (Giglio et al., 2016; Schroeder et al., 2014; Wooster et al., 2012; Xu et al., 2020) offer the capability to observe and quantify wildfire activity using Active Fire (AF) approaches involving FRP retrievals. Well-known inventories using these methods include the Fire Inventory from NCAR (FINN, Wiedinmyer et al., (2011)), the Fire Energetic and Emission Research (FEER) approach (Ichoku and Ellison, 2014)), the Quick Emission Dataset (QFED, Darmenov and da Silva, (2015)), and GFAS (Kaiser et al., 2012). The most recently developed FREM method (Nguyen et al., 2023) directly links satellite-derived FRP data to a fires CO emission rate via a set  $EC_{CO}^b$  derived from a 'matchup fire' subset of satellite-derived FRP and CO observations. Specifically, estimates of  $EC_{CO}^b$  are calculated using FRE and plume-integrated Total Column Carbon Monoxide (TCCO) data collected at a subset of 'matchup fires' where both datasets are 'well-observed' (e.g. no gaps in the FRP record, and a clear fire emissions CO plume is seen). Once derived, application of  $EC_{CO}^b$  to the FRP observations at all the regions fires enables the regions fire-related CO emission rates to be calculated without the need for any other information (Reid et al., 2009). Hence the approach is extremely direct, and with the emissions coefficients derived from the same types of satellite FRP data that they will ultimately be applied to, and thus which are impacted by the same factors such as overstory impacts on FRP measures and minimum FRP detection limits (Nguyen and Wooster, 2020).

Each FREM iteration thus far has relied on geostationary FRP data, due to its frequent 10-to-30 min imaging frequency enabling easy derivation of FRE (Wooster et al., 2021). Rather than CO however, the first FREM (v1) iteration focused on deriving aerosol optical depth (AOD) related total particulate matter (TPM) emissions from FRP observations (Mota and Wooster, 2018), an approach then enhanced by Nguyen and Wooster, (2020) and Fisher et al., (2020) through the use of improved AOD datasets. FREMv2 (Nguyen et al., 2023) replaced use of AOD data with trace gas column amounts of CO (from the S5P satellites TROPOMI instrument), directly estimating fluxes of CO rather than TPM. CO is the second largest fire-emitted compound after CO<sub>2</sub> (Akagi et al., 2011) and CO emissions factors are significantly less variable than those of



130

140

158

159



- 128 TPM (Andreae, 2019). This makes any subsequent estimation of total fuel consumption using the FREM approach more
- 129 appropriately conducted using CO pathway rather than one based on TPM fire emissions data.

#### 3. High Latitude FREM Adaptation

al., 2023; Nguyen and Wooster, 2020).

131 The polar-orbiting based HLFREM framework developed herein builds on the geostationary FREM methods by identifying a set of matchup fires for which both the total amount of CO contained in the fire plume is assessed, as well as the total amount 132 of FRE released over the time it took the plume to form. Using these polar-orbiting matchups, a set of  $EC_{CO}^{b}$  are generated 133 134 using ordinary least squares (OLS) linear best fits to the co-incident FRE and CO data of all matchup fires in that biome. These 135  $EC_{GO}^{b}$  can then be multiplied by the regionally complete FRP time-series, including potentially hundreds of thousands more fires than are included in the matchup datasets, generating a spatially and temporally comprehensive set of biomass burning 136 CO emissions covering all fires. Dividing these CO emissions by the standard biome-specific Emissions Factors (EFs, (Akagi 137 et al., 2011; Andreae, 2019)) provides estimates of dry biomass consumption and also of total carbon (assuming biomass is 138 139  $50\% \pm 5\%$  carbon), or via use of EF ratios of any trace gas to CO also estimates of other trace gas emissions totals (Nguyen et

The regionally comprehensive FRP time-series used herein is the Global Fire Assimilation System (GFAS v1.2) FRP dataset described in (Kaiser et al., 2012), generated as part of the Copernicus Atmospheric Monitoring Service (CAMS: https://atmosphere.copernicus.eu/) and widely used (e.g. Di Giuseppe et al., 2018; Inness et al., 2019; Popovicheva et al., 2022)
The GFAS v1.2 record is based on per-pixel FRP retrievals contained within the Terra/Aqua MOD14/MDY14 active fire products (Giglio et al., 2016), using these to generate daily mean cloud-adjusted FRP data gridded at 0.1° back to almost the start of the MODIS mission (Kaiser et al., 2012).

147 However, whilst the GFAS v1.2 FRP data dating back to 2003 are considered a suitably long FRP time-series for generating a long-term CO emissions record, they are less well suited to the initial generation of the  $EC_{CO}^{b}$  coefficients linking FRP to rate 148 of CO emissions since they provide only daily average FRP values. Specifically, the daily average FRP data contained in 149 GFAS v1.2 cannot be used to estimate the amount of FRE emitted by a fire from the night-time FRP minimum up until the 150 151 early afternoon TROPOMI overpass, since only daily average FRP is provided, and yet this sub-daily FRE value is required at the set of matchup fires to generate the initial  $EC_{CO}^b$  emissions coefficients. For this reason, these coefficients were instead 152 derived using the alternative GFAS v1.4 implementation (Kaiser et al., 2024), which applies the fire diurnal cycle model of 153 154 (Andela et al., 2015) to the 0.1° gridded MODIS FRP used to generate GFAS v1.2 but now to obtain hourly gridded FRP 155 estimates. At the location of each matchup fire, these hourly FRP data can then be integrated over the required time period 156 from the night-time fire minimum up until the S5P (TROPOMI) satellite overpass time to generate the FRE released. Though GFAS v1.4 goes back only to 2019, this is perfectly sufficient for deriving the  $EC_{CO}^b$  coefficients. 157

The full selection process for the fire matchups to which this procedure is applied is described in Sect. 3.2; and at each fire the relevant FRE was calculated as described in Sect. 3.3 using as the temporal integration period the time between the early



167

168169

170

171

172173

174

175



morning fire activity minimum and the S-NPP VIIRS overpass made almost simultaneously to that of S5P (Sect. 3.4). Once sufficient matchup fires existed for each fire biome covered (see Sect. 3.5), we generated  $EC_{CO}^b$  for these biomes as detailed in Sect. 3.6. These emission coefficients were then multiplied by the full GFAS v1.2 FRP record (Jan 2003 – Dec 2024, Sect. 4.1), to generate a HLFREM CO emission timeseries. Additionally, via the application of the appropriate EFs, it was also possible to generate a HLFREM Carbon emission timeseries using GFAS v1.2 (Sect 4.2). For both the CO and Carbon emission timeseries, the HLFREM emissions will be compared to pre-existing emission databases; namely FEER, GFAS v1.2, and GFED v4.1s.

# 3.1. Region of Interest Selection

HL fire is seasonal in nature, dominantly present in the Northern Hemispheric Summer months (June, July, August, Fig. 2a). Four HL ROIs and matching time periods were used from within this period to generate the set of matchup fire, and each of the ROI extractions focused on a period when fire activity was maximised in that ROI, as shown in Figs. 2b and 2c, and detailed in Table 1. Landcover data, natively at 300 m grid resolution, taken from the ESA Climate Change Initiative (ESA-CCI) 2018 land cover map (ESA, 2017) was used to classify biomes within the ROI's, based on 11 'fire-biome' classes aggregated from the original 37 landcovers (Table A1), as shown in Fig. 2b. The two ROIs in Boreal Asia (HL-BOAS-20 and HL-BOAS-21) were dominated by the Deciduous Needleleaf Forest fire biome, whereas those in Boreal North America (HL-BONA-19 and HL-BONA-23) were dominated by Evergreen Needleleaf Forest fire biome.



178

179

180

181

182

184

185



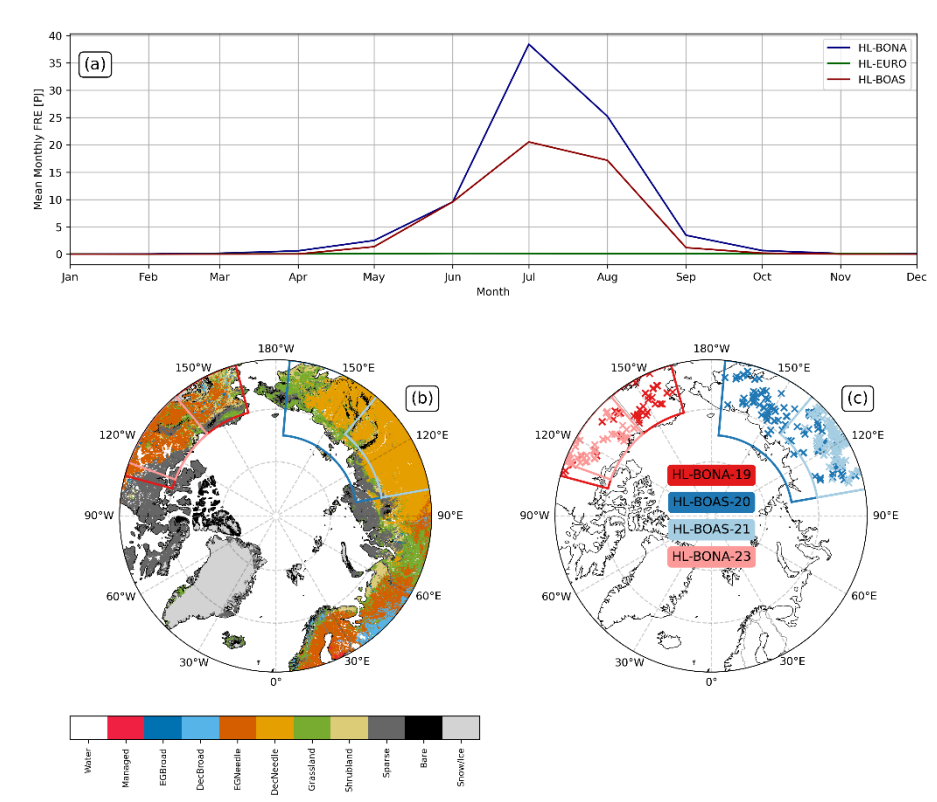


Figure 2: HL fire information. (a) Mean monthly FRE (2003 – 2024) for HL fires ( $\geq$  60°N) in the regions used by the Global Fire Emissions Database (GFED; (Randerson et al., 2017), BONA: Boreal North America, EURO: Europe, BOAS: Boreal Asia), as derived from GFAS v1.2. (b) ROI and aggregated fire biome map, as derived from the CCI Land Cover 2018 map (ESA, 2017) and with biome aggregation detailed in Table A1. (c) The four ROIs used in this study within which the 833 fire-matchup (shown as crosses) were identified.

Table 1: Acronyms and Geographic bounding boxes of ROIs, as shown in Fig. 2c.

ROI Full Name	ROI Acronym	Bounding Box
High Latitude Boreal North America 2019	HL-BONA-19	60° N - 70° N, 105° W - 165° W
High Latitude Boreal Asia 2020	HL-BOAS-20	60° N - 75° N, 100° E - 175° E
High Latitude Boreal Asia 2021	HL-BOAS-21	60° N - 70° N, 100° E - 140° E
High Latitude Boreal North America 2023	HL-BONA-23	60° N - 70° N, 100° W - 140° W

#### 183 3.2. Data Used and Plume Identification

Within each of the four ROIs shown in Figs. 2b and 2c, the potential cloud-free matchup fires were manually identified and examined via visual inspection of multispectral and AF Products detailed in Table 2, based on the following criteria:



187

188

189

190

191

192

193

194



- Clear smoke emission visible in the VIIRS true colour (Red: M05, Green: M04, Blue: M03) imagery, and without apparent mixing with other nearby smoke plumes.
- Clear visual indication of a developed smoke plume, spread by the wind, in the same VIIRS true colour imagery.
- Clear identification of a region of shortwave infrared thermal emission (hereby referred to as the "burning area") resulting from active combustion, as seen in a VIIRS false colour (Red: M11, Green: I02, Blue: I01) imagery.
- AF Pixels present within the "burning area" as deduced from the VIIRS VNP14 and MODIS MOD14/MYD14 AF
   Products.

Table 2: Satellite data products used during the manual inspection and digitization of matchup fire polygons.

Parameter	Satellite	Product Code	Resolution (nadir)
VIIRS Moderate Resolution L1B Calibrated Radiances	S-NPP	VNP02MOD	750 m x 750 m
VIIRS Moderate Resolution L1B Terrain Corrected Geolocation	S-NPP	VNP03MOD	750 m x 750 m
VIIRS Imagery Resolution L1B Calibrated Radiances	S-NPP	VNP02IMG	375 m x 375 m
VIIRS Imagery Resolution L1B Terrain Corrected Geolocation	S-NPP	VNP03IMG	375 m x 375 m
VIIRS Thermal Anomalies/Fires	S-NPP	VNP14v002	750 m x 750 m
MODIS Thermal Anomalies and Fire	TERRA	MOD14v001	1.0 km x 1.0 km
MODIS Thermal Anomalies and Fire	AQUA	MYD14v001	1.0 km x 1.0 km
VIIRS Enterprise Processing System Aerosol Optical Depth	S-NPP	AOD EPS	750 m x 750 m
TROPOMI Level 2 Total Column Carbon Monoxide	Sentinel-5P	L2_CO	7.0 km x 3.5 km

Each potential matchup fire then had its smoke plume and associated burning area extent digitized and examined; based on manual interpretation of the VIIRS multispectral imagery, matching VIIRS AF and Aerosol optical depth (AOD) products (NOAA, 2020), and TROPOMI TCCO products, as shown in Fig. 3.



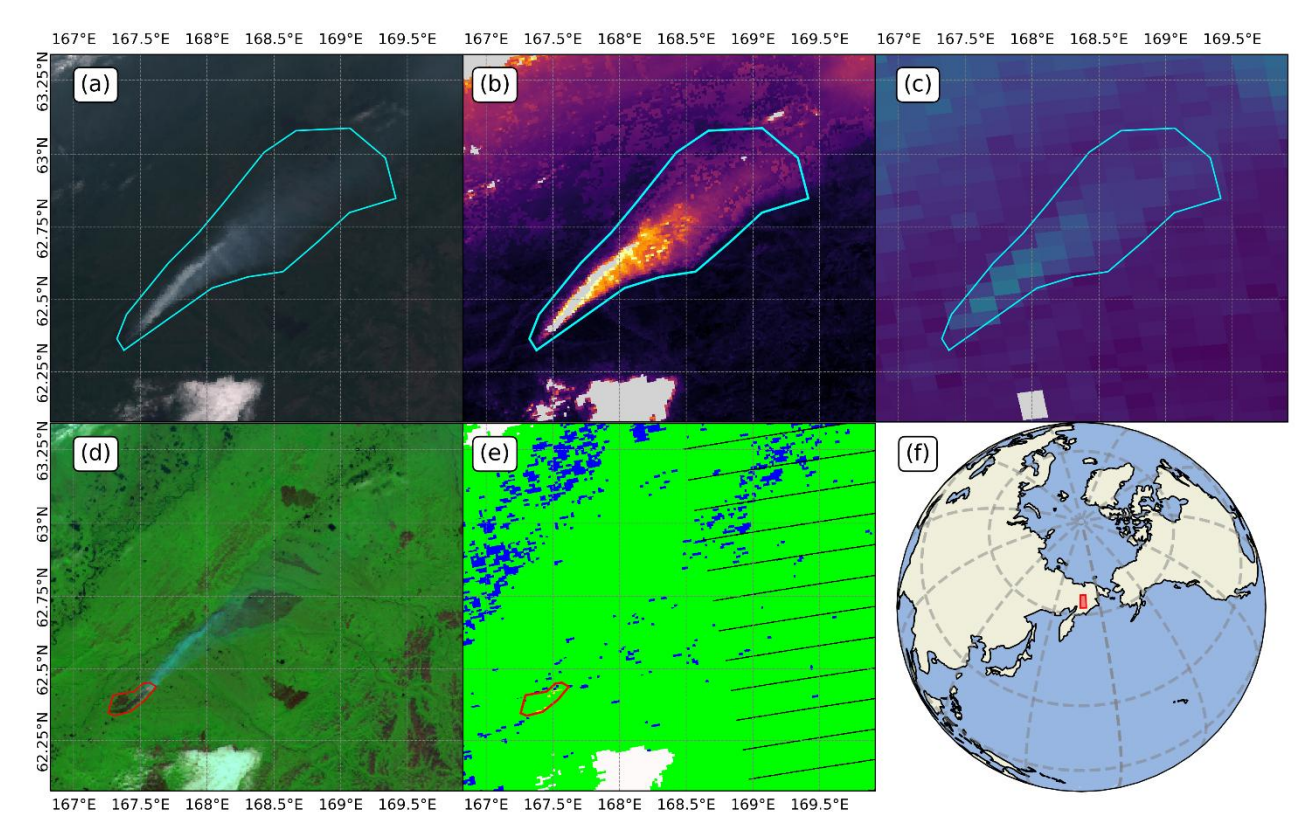


Figure 3: Example of a matchup fire imaged in Siberia (62.39° N, 167.49° E) on 28/07/2020 at 01:42 UTC (13:42 PETT). The digitised outline of the plume (cyan) and burning area (red) are shown superimposed on (a) RGB (M05-M04-M03) imagery via S-NPP (VIIRS), (b) AOD (processed via EPS) from S-NPP (VIIRS), (c) Sentinel-5P TCCO data, (d) False Colour Composites (M11-I02-I01) via S-NPP (VIIRS), (e) VIIRS Active Fire Product (VNP14) from S-NPP (VIIRS). Green: Non burning vegetation. Yellow: Active Fire Hotspot, Blue: Water, White: Cloud, Black: No Data. (f) Geographic location and extent of the plots shown (red).

#### 3.3. Fire Radiative Energy Estimation

To calculate the FRE for each matchup fire, each digitised burning area polygon was converted to a binary mask and used to extract the FRP time-series from the hourly-timestep FRP record held within GFAS v1.4 (see example in Fig. 4). HL orbital convergence ensured the calculation was based on significantly more polar-orbiting observations than would be the case at lower latitudes (Fig. 1), and, following (Nguyen et al., 2023), the FRP integration took place from the 06:00 hrs local time fire activity minima (Fig. A1) up until the time of the almost simultaneous early afternoon S5P and Suomi S-NPP overpasses. Mean FRP record length for all matchup fires was 7.3 hrs (minimum 4 and maximum 11 hours), with the variation due to the orbital convergence (Fig. 1) and this results in the match-up fires being observed by Sentinel-5P up to three times per day from different ascending overpasses.





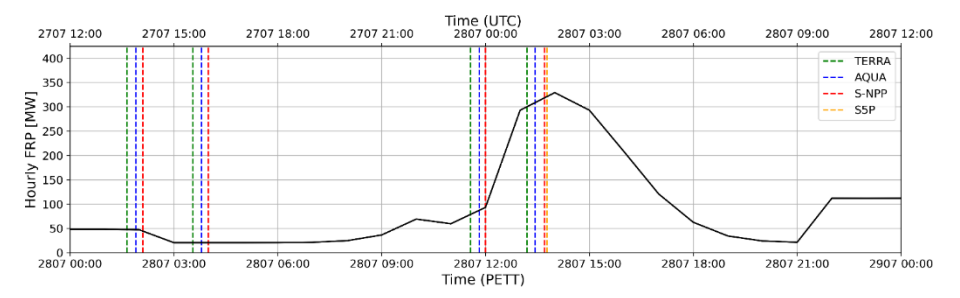


Figure 4: Example of the hourly FRP time-series from GFAS v1.4, used to generate an FRE measure for a single matchup fire (i.e. the match-up fire in Fig. 3, as shown above). The hourly FRP timeseries data were generated from the set of individual FRP observations provided by MODIS on AQUA and TERRA, using the diurnal cycle model of Andela et al., (2015). Additionally, the VIIRS observations on S-NPP used for fire-matchup identification are also shown. Times of the individual satellite overpasses, as well as of the S5P overpass time used to provide the TCCO data for this fire-matchup, are indicated.

#### 3.4. Excess CO Estimation

For each fire-matchup, the smoke plume polygon with a surrounding buffer of one pixel was also used to generate a binary mask employed to extract the relevant S5P TROPOMI TCCO data within the plume, along with a measure of the ambient background TCCO ( $TCCO_{BG}$ , taken as the minimum TCCO within the buffered mask). Total excess plume CO ( $CO_{EX}$ ) was then calculated for each fire-matchup, as the sum of all  $CO_{EX}$  from each S5P pixel associated with each fire-matchup, using Eq. (1).

$$CO_{Ex} = \sum (TCCO_{M} - TCCO_{BG}) \cdot A \cdot M_{CO}$$
 (1)

where  $TCCO_M$  is the TCCO within the buffered binary mask (units: mol m<sup>-2</sup>),  $TCCO_{BG}$  is the ambient background TCCO (units: mol m<sup>-2</sup>), A is the S5P pixel size (units: m<sup>2</sup>) calculated from the geographic coordinates of the pixel corners, and  $M_{CO}$  the molecular weight of CO (units: g mol<sup>-1</sup>).

#### **3.5. Fire Biome Estimation**

All MODIS and S-NPP AF pixels within the fires burning area polygon and timed during the FRP temporal integration period had their fire-biome determined using the aggregated biome data shown in Fig. 2b. For a single fire if  $\geq 50\%$  of the AF pixels were from a single fire-biome then that was set as the fires "dominant" fire-biome. Fires having no such dominant class were discarded, as their derived emission coefficients could not be properly allocated to a fire-biome.

### 3.6. Biome Specific Emission Coefficient Generation

In total, 833 individual matchup fires were initially identified, with 125 of those being discarded as having no dominant fire-biome. Of the 708 fires remaining, 468 were located in Deciduous Needleleaf Forest (DecNeedle), 186 in Evergreen Needleleaf Forests (EGNeedle), 26 in Grassland, 22 in Shrubland, and six in a fire-biome described as 'Sparce'. The locations





of the matchup fires for the four most well-sampled fire-biomes identified (DecNeedle, EGNeedle, Grassland, and Shrubland) are mapped in Fig. 2c. Analysis of the mean annual FRE totals from GFAS v1.2 (Fig. 5, Table 3) shows that these four biomes are responsible for the vast majority (~93%) of the total FRE generated by HL fires.

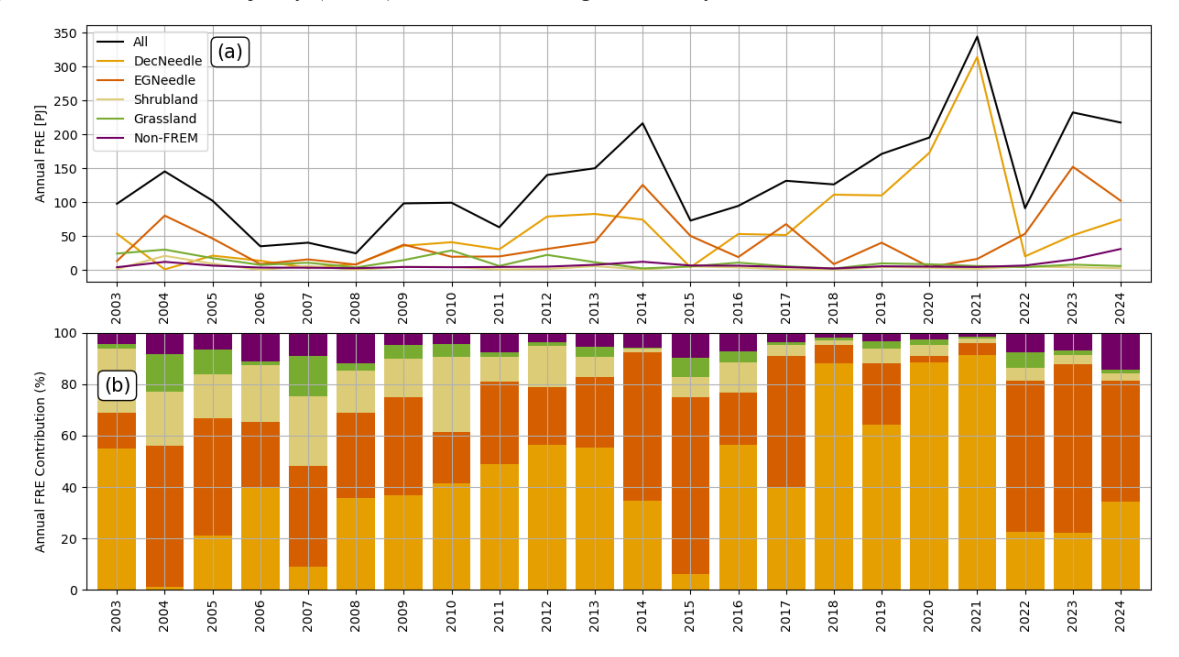


Figure 5: Mean annual HL FRE (a) totals (PJ), and (b) contribution (%) of each of the four most well sampled biomes identified as part of the fire-matchups database, as well as from additional biomes, taken from GFAS v1.2 (2003-2024).

Table 3: Mean Annual FRE totals (PJ) and contribution (%) for each of the four most well sampled biomes, compared to all other HL biomes, calculated using GFAS v1.2, between 2003 and 2024.

HL Biome	Mean Annual FRE Total (PJ)	Standard Deviation (PJ)	Mean annual FRE Contribution (%)	Standard Deviation (%)
All	205.4	115.5	100	0.0
DecNeedle	100.2	106.9	43.0	24.7
EGNeedle	67.8	59.9	34.2	19.1
Grassland	17.9	12.4	11.6	8.4
Shrubland	6.7	6.0	4.2	4.1
All other biomes	12.8	9.9	7.0	3.3

Following Nguyen et al., (2023), the FRE and Excess CO data of each fire-biomes matchup fires were used to derive a set of  $EC_{CO}^b$  emissions coefficients via zero-intercept OLS linear regression (Fig. 6); with results reported in Table 4. As detailed in Nguyen and Wooster, (2020), "FEER-equivalent"  $EC_{CO}^b$  values are also reported therein, calculated from the grid cell (not biome) based FRP-based total particulate matter (TPM) emissions coefficients ( $EC_{TPM}^b$ ) reported in Ichoku and Ellison,





250 (2014) (available at www.feer.gsfc.basa.gov/data/emissions/) and the relevant biomes TPM-to-CO EF ratios (Nguyen and

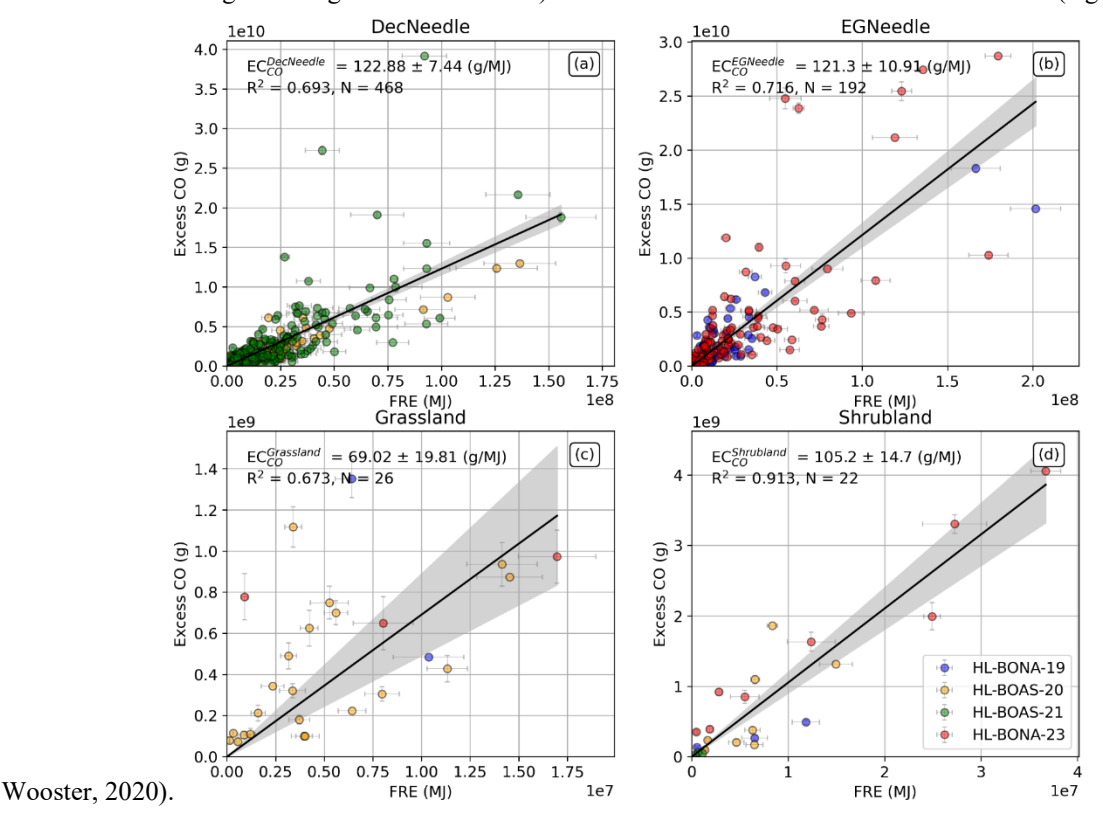


Figure 6: HLFREM biome-specific CO emission coefficients ( $EC_{CO}^b$ , in g MJ<sup>-1</sup>) derived from the set of matchup fires for (a) Deciduous Needleleaf Forests, (b) Evergreen Needleleaf Forests, (c) Grasslands, and (d) Shrubland fire-biomes. Each datapoint represents a single matchup fire that had its plume total Excess CO and total released FRE assessed for a matching time-period, and the  $EC_{CO}^b$  value for the fire-biome is derived from the slope of the OLS linear best fit (solid black line) to these data. Colour of the scatter points denotes the ROI containing the fire (see Fig. 2c). Error bars denote the standard deviation of FRP values and the uncertainty in the S5P TCCO produce respectively, as calculated following (Nguyen et al., 2023). The shaded area indicates the uncertainty on the slope of the linear best fit, taken to be the uncertainty on the derived  $EC_{CO}^b$  value.

Table 4: Emissions coefficients for CO  $(EC_{CO}^b)$  as derived in Fig. 6, along with FEER-equivalent values for comparison and those for carbon  $(EC_C^b)$  calculated using  $EC_{CO}^b$  and EFs from (Andreae and Merlet, 2001) and (Akagi et al., 2011) - labelled -AM, and -AG respectively, in Sect. 4.2.

HLFREM Biome	Sentinel-5P TCCO-derived EC <sub>CO</sub> [g MJ <sup>-1</sup> ]	FEER-equivalent $EC_{CO}^{b}$ [g MJ <sup>-1</sup> ]	Sentinel-5P TCCO-derived EC <sub>C-AM</sub> [g MJ <sup>-1</sup> ]	FEER-equivalent $EC_{C-AM}^b$ [g MJ <sup>-1</sup> ]	Sentinel-5P TCCO-derived $EC_{C-AG}^{b}$ [g MJ <sup>-1</sup> ]
DecNeedle	122.88	198.3	553.84	893.7	449.90
EGNeedle	121.30	169.5	546.71	764.1	444.12
Grassland	69.02	198.3	311.08	893.7	252.71
Shrubland	105.20	151.7	474.2	683.8	385.17





# 4. Emission Inventory Comparisons

#### 4.1. High Latitude Carbon Monoxide Emission Timeseries

To generate a long-term CO emissions timeseries for the HL biomes, we applied the derived  $EC_{CO}^b$  emissions coefficients to the GFAS v1.2 FRP data available from the current time back to almost the start of the MODIS record (2003). The resulting monthly and annual CO emissions timeseries are shown in Fig. 7. Also shown are the FEER-equivalent CO timeseries, the CO emissions that come as part of the GFAS v1.2 dataset derived from the FRP values as per Kaiser et al., (2012), and the GFED v4.1s CO emissions (2003 – 2023). The mean annual CO emissions for the four biomes using HLFREM, FEER, GFAS v1.2, and GFED v4.1 can be found in Table 5, and note that of these four datasets, the same MODIS FRP data drive the emissions estimates in HLFREM, GFAS v1.2 and FEER, whilst GFED v4.1s uses primarily MODIS burned area data (Giglio et al., 2013). However, also note that the conversion coefficients linking daily mean FRP to biomass burned in GFED v1.2 as a prior step to its CO emissions estimation were generated using linear regression against burned biomass estimates of an earlier version of GFED (Kaiser et al., 2012). HLFREM removes this link by directly relating the daily FRP measures to CO fluxes via the conversion coefficients derived from FRP and Sentinel-5P CO data at the matchup fires.

Table 5: Mean annual (2003-2023) CO emissions for the inventory-biome pairs. Uncertainty values are the standard error of the mean.

Inventory	DecNeedle	EGNeedle	Grassland	Shrubland
HLFREM	$7.83 \pm 1.92 \text{ Tg}$	$5.00 \pm 1.03 \text{ Tg}$	$0.81 \pm 0.13 \text{ Tg}$	$0.46\pm0.10~Tg$
FEER	$12.64 \pm 3.10 \ Tg$	$6.99 \pm 1.43 \; Tg$	$2.33 \pm 0.37 \; Tg$	$0.67 \pm 0.15 \; Tg$
GFAS v1.2	$11.48 \pm 2.66 \ Tg$	$7.18 \pm 1.39 \; Tg$	$4.03\pm0.80\;Tg$	$0.80 \pm 0.16 \; Tg$
GFED v4.1s	$13.63 \pm 4.07 \ Tg$	$8.74 \pm 2.23 \ Tg$	$2.12 \pm 0.32 \; Tg$	$0.68 \pm 0.16 \; Tg$





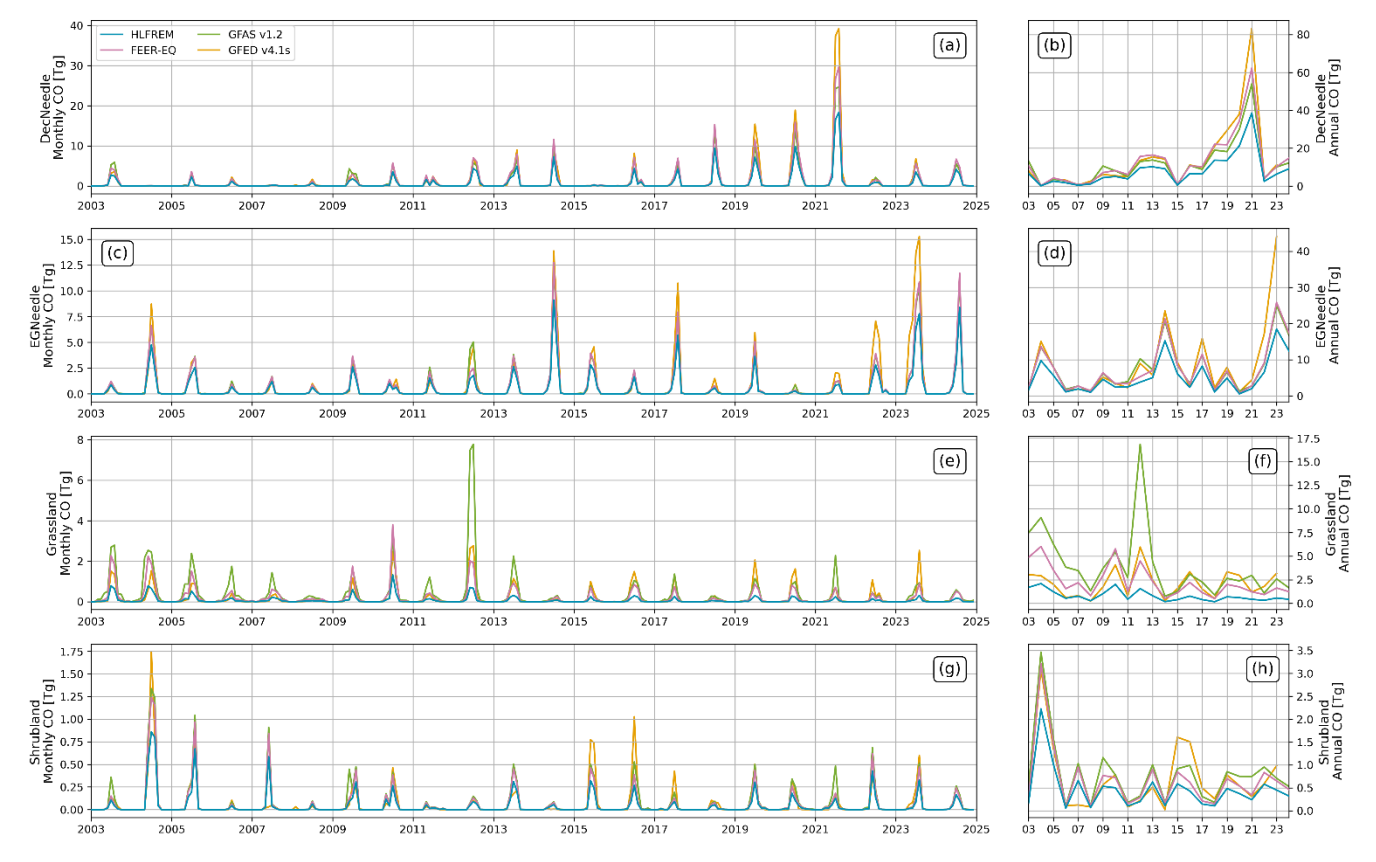


Figure 7: Timeseries of Monthly (a,c,e,g) and Annual (b,d,f,h) HL Wildfire emissions of CO for (a,b) DecNeedle, (c,d) EGNeedle, (e,f) Grassland, and (g,h) Shrubland biomes, calculated using the  $EC_{CO}^b$  from HLFREM (blue) and FEER (orange) as detailed in Table 4 using daily FRE totals generated by GFAS v1.2. GFAS v1.2 (green) and GFED v4.1s (red) CO emissions for the same biomes are shown in green. OLS regression analysis can be found in Fig. A2.

It can be seen from Fig. 7 that the temporal patterns of HLFREM CO emissions across all biomes are consistent with those from the other three inventories, with the temporal patterns being more pronounced in the two forested and Shrubland biomes. The peaks also match independent reports of fire activity, for example with the DecNeedle biome showing CO peaks in both 2020 and 2021 consistent with the high fire activity reported across HL Russia (dominated by DecNeedle) in these years (Kharuk et al., 2021; Ponomarev et al., 2021). Similarly, the CO increase in 2023 in the EGNeedle biome is consistent with reported high fire activity across HL North America (Byrne et al., 2024; Dodd et al., 2018). It is clear from Fig. 7 and Table 5 that the CO emissions from HLFREM across the two forested biomes are consistently smaller than those of the other inventories (DecNeedle: 38%, 32%, and 43% smaller than FEER, GFAS v1.2, and GFED v4.1s respectively, EGNeedle: 28%, 30% and 43% smaller than FEER, GFAS v1.2, and GFED v4.1s respectively). The HLFREM CO emissions for Shrublands are also smaller by the same magnitude (31%, 43%, and 33% smaller than FEER, GFAS v1.2, and GFED v4.1s respectively). For Grasslands, however, the HLFREM CO emissions are significantly smaller (65%, 80%, and 62% smaller than FEER, GFAS v1.2, and GFED v4.1s respectively), though the grassland  $EC_{CO}^b$  emission coefficient (Fig. 6c) has a smaller r2 value,





potentially making them more uncertain. Additionally, there appear to be some unusual patterns in the Grassland biome; the CO emissions from GFAS v1.2 exhibit a peak in June and July 2015 and July 2021, peaks not seen in the HLFREM- nor FEER-derived versions. On investigation, these peaks are due to an above-average number of grassland fires occurring in regions defined within GFAS as having peat (Kaiser et al., 2012), as opposed to extratropical forests with organic soils (EFOS). The presence of peat dramatically increases the conversion factor linking FRP to dry matter combustion in the GFAS system via the linear regression performed against GFED biomass burned estimates (Kaiser et al., 2012). Therefore, in the GFAS v1.2 CO emissions dataset, the same FRE values for grassland fires in these 'PEAT' regions results in significantly more CO than identical FRE fires in the EFOS regions. The HLFREM and FEER-equivalent inventories do not make this distinction, and so their CO timeseries do not show such elevated CO emissions peaks related to differing Grassland fire locations. Figure 8 shows the fractional dominant fire type as denoted by GFAS v1.2 and GFED v3.1 for the four HL biomes used in this study. The Grassland biome has a larger fraction of PEAT (11.7%), compared to the other three biomes (DecNeedle: 2.8%, EGNeedle: 1.6%, Shrubland: 3.1%). Nevertheless, since that CO emissions from fires in Grassland only represent ~12% of the multi-biome total FRE (Table 3) the overall impact of this difference is limited on the total CO emissions values.

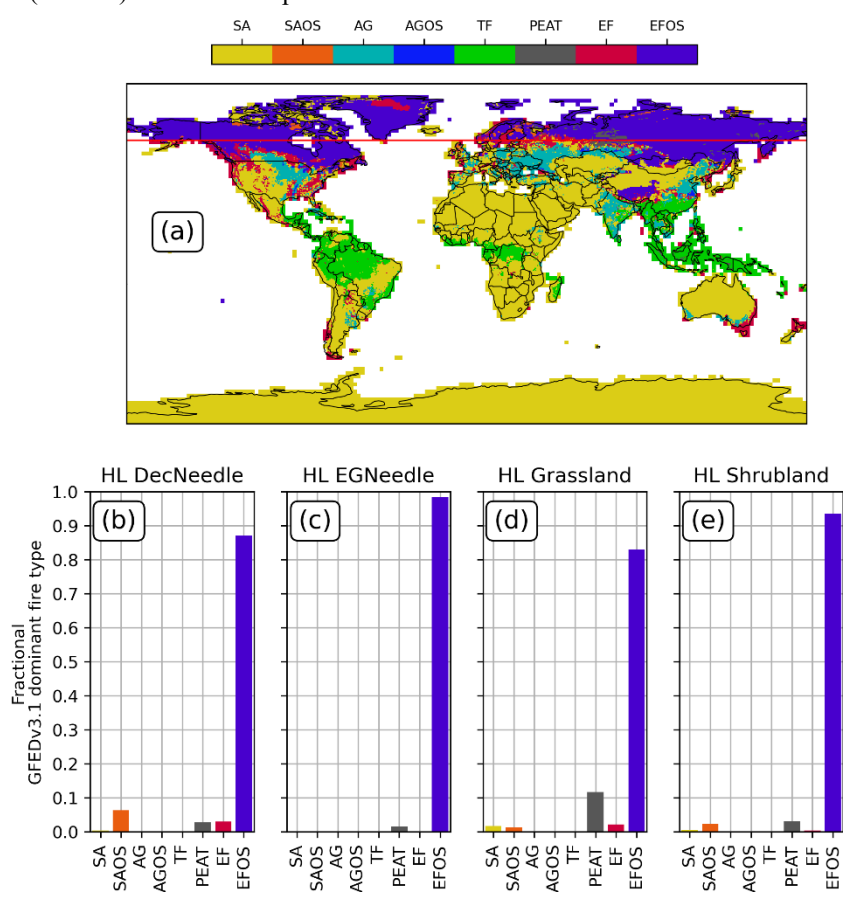


Figure 8: GFAS v1.2 land cover classes, based on dominant fire type in GFED v3.1 and organic soils and peat maps, taken from (Kaiser et al., 2012). (a) Land cover classes map, for Savannah (SA), Savannah with organic soils (SAOS), Agriculture (AG),





Agriculture with organic soils (AGOS), Tropical Forest (TF), Peat (PEAT), Extratropical Forest (EF), and Extratropical Forests with organic soils (EFOS). 60°N is denoted with a red line. (b-e) Fractional land cover for (b) HL DecNeedle, (c) HL EGNeedle, (d) HL Grassland, and (e) HL Shrubland.

In terms of spatial patterns, Fig. 9 maps the annual total GFAS v1.2 FRE values for the HL-BONA-2023 and HL-BOAS-2021 ROIs, detailed in Table 1, from which the HLFREM  $EC_{CO}^b$  were derived from. The elevated annual FRE totals (Figs. 9a and 9b) align with CO emissions across all four inventories (Figs. 9c-h), whose spatial pattern is very similar, and corresponded to the extreme wildfire activity reported in these years and regions (Byrne et al., 2024; Kharuk et al., 2021).

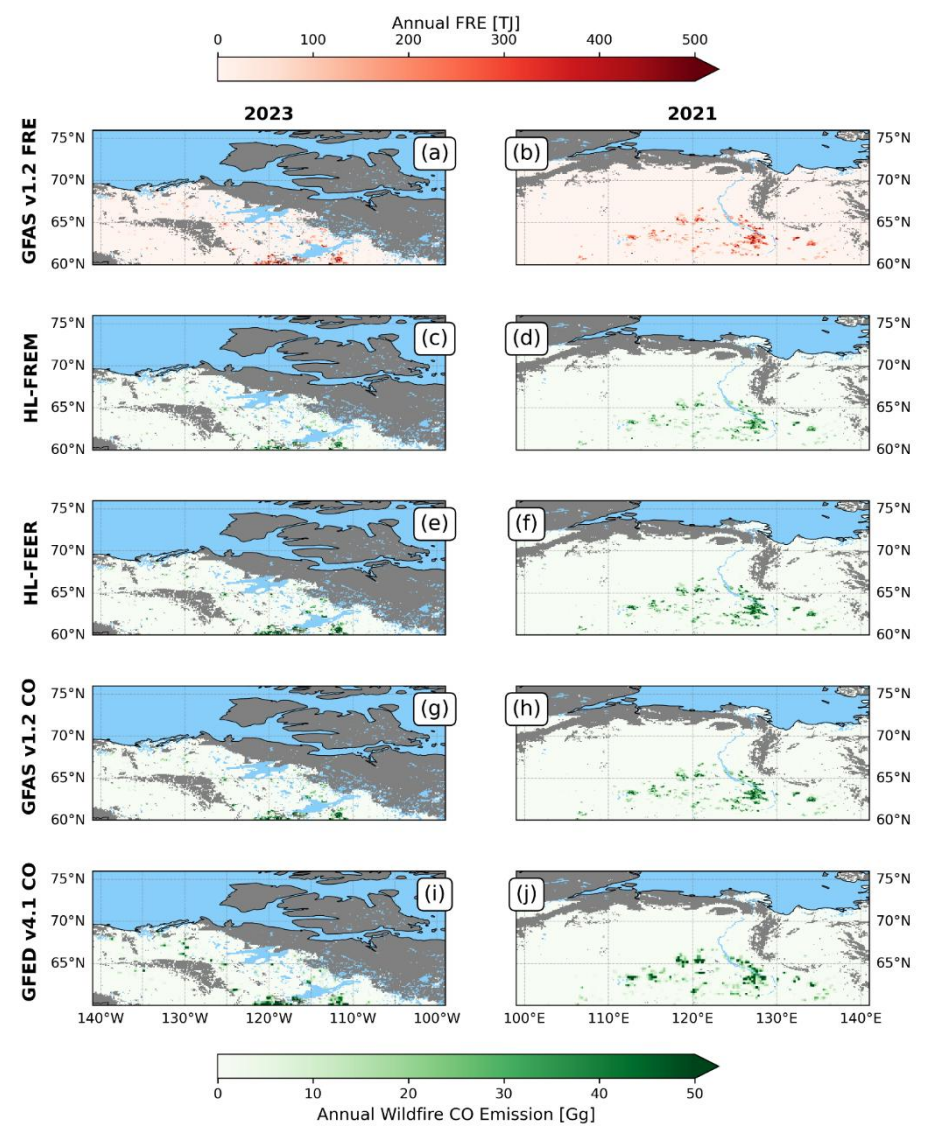


Figure 9: Annual FRE totals from GFAS v1.2 (a, b) and CO emissions (c-j) for the HL-BONA-23 (a, c, e, h, i) and HL-BOAS-21 (b, d, f, h, j) ROIs from the HLFREM (c, d), FEER-equivalent (e, f), GFAS v1.2 (g, h), and GFED v4.1s (i, j), respectively. Grey areas denote regions that do not fall under one of the four HLFREM biomes.





## 4.2. High Latitude Carbon Emission Timeseries

Following the approach of (Mota and Wooster, 2018; Nguyen et al., 2023; Nguyen and Wooster, 2020), emissions estimates of total carbon, as well as any other GHG or trace gas, can be derived from the CO emissions provided by the HLFREM approach, simply via use of standard ratios of the relevant gaseous emission factors. Numerous different summarised EF inventories exist, with for example GFAS v1.2 using (Andreae and Merlet, 2001) and GFEDv4.1s using (Akagi et al., 2011). HL wildfire emissions of Carbon, for example, can be calculated using its biome-specific emission coefficient ( $EC_c^b$ ), derived using the EF ratio between Carbon and CO, and the HLFREM CO emission coefficient ( $EC_{CO}^b$ ), via Eq. (2):

$$EC_C^b = \frac{EF_C^b}{EF_{CO}^b}EC_{CO}^b \tag{2}$$

Where the emission coefficients have units: g MJ<sup>-1</sup> and the emission factors units: g kg<sup>-1</sup>.  $EF_{CO}^b$  values are taken from the aforementioned emission inventories, and  $EF_C^b$  being calculated using Eq. (3):

$$EF_C^b = \frac{12}{44}EF_{CO_2}^b + \frac{12}{28}EF_{CO}^b + \frac{12}{16}EF_{CH_4}^b$$
(3)

Where  $EF_C^b$ ,  $EC_{CO_2}^b$ ,  $EC_{CO_2}^b$ , and  $EC_{CH_4}^b$  are the biome specific wildfire EFs for burnt carbon, CO<sub>2</sub>, CO, and CH<sub>4</sub> respectively, assuming these make up more than 95% of burnt carbon emitted in gaseous form (Akagi et al., 2011) and that by comparison carbon in aerosols is negligible by mass (Akagi et al., 2011; Andreae and Merlet, 2001). Multiplying these carbon emissions by a factor of two then provides an estimate of the amount of biomass burned.

Similar to Fig. 7, Fig. 10 shows our multi-inventory Carbon emissions calculated across the four most dominant HL fire affected biomes. As GFAS v1.2 uses EFs from Andreae and Merlet, (2001), we calculated  $EC_C^b$  for both HLFREM and FEER using these same EFs, as shown in Table 4. However, as GFED v4.1s uses EFs from (Akagi et al., 2011), we also calculated  $EC_C^b$  for HLFREM using these same EFs, also shown in Table 4. The HLFREM and FEER  $EC_C^b$  were applied to the GFAS v1.2 daily FRE totals, and, similar to Table 5, mean annual HL Wildfire Carbon emissions totals were calculated, and are shown in Table 6.

The HLFREM carbon emission timeseries exhibits a very similar behaviour as the CO emission timeseries from which it was derived; with a strong temporal similarity with the carbon emissions of the other inventories. The difference between the HLFREM carbon emissions and the other inventories for the two forested biomes (DecNeedle: 38%, 30%, and 42% smaller than FEER, GFAS v1.2, and GFED v4.1s respectively, EGNeedle: 28%, 30% and 42% smaller than FEER, GFAS v1.2, and GFED v4.1s respectively) and the Shrubland biomes (31%, 41%, and 32% smaller than FEER, GFAS v1.2, and GFED v4.1s respectively), are very similar to those of the CO emissions, differing by  $\leq$  2% from these. The HLFREM carbon emission timeseries from Grassland also exhibits a similar behaviour to those of the Grassland HLFREM CO emission timeseries (65%, 74%, and 61% smaller than FEER, GFAS v1.2, and GFED v4.1s respectively); in that the emission estimations are significantly smaller than those from the other inventories, although the difference from GFAS v1.2 (6%) is larger than those from the other two inventories (2%).





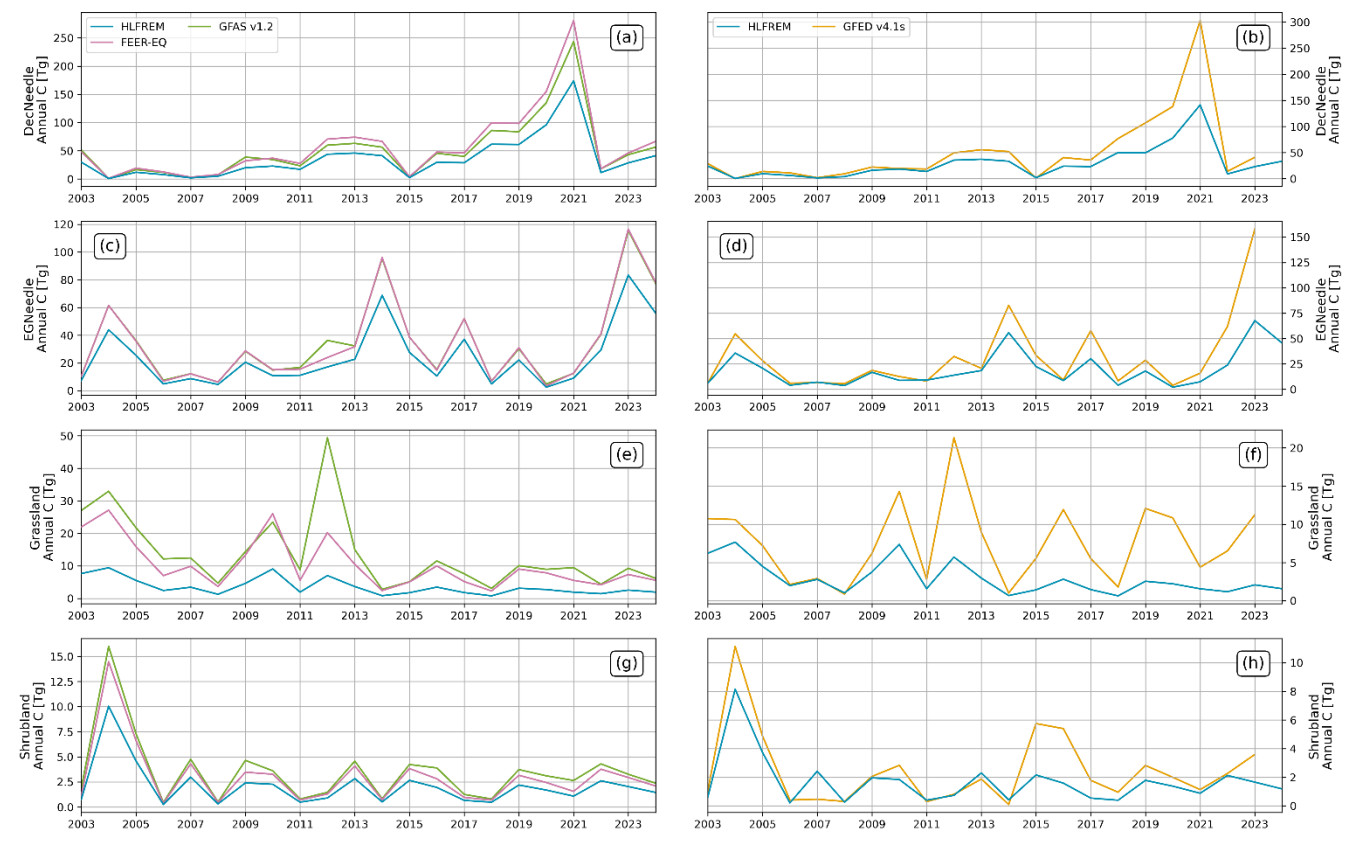


Figure 10: Timeseries of HL Wildfire Emissions of Carbon for (a, b) Deciduous Needleleaf Forest, (c, d) Evergreen Needleleaf Forest, (e, f) Grasslands, and (g, h) Shrublands biomes, for (a, c, e, g) FEER, GFAS v1.2, and HLFREM (using EFs from (Andreae and Merlet, 2001)), and (b, d, f, h) GFEDv4.1s and HIFREM (using EFs from (Akagi et al., 2011)). Regression analysis on the timeseries can be found in Fig. A3.

Table 6: Mean annual (2003-2023) C emissions for the inventory-biome pairs. HLFREM<sub>AM</sub> details the mean annual HL Carbon emissions, using  $EC_{C-AM}^b$ , whilst HLFREM<sub>AG</sub> details the mean annual HL Carbon emission using  $EC_{C-AG}^b$ . HLFREM and FEER HL Carbon emissions are generated using GFAS v1.2 FRE totals. Uncertainty values are the standard error of the mean.

Inventory	DecNeedle	EGNeedle	Grassland	Shrubland
HLFREM <sub>AM</sub>	$35.29 \pm 8.67 \text{ Tg}$	$22.53 \pm 4.62 \text{ Tg}$	$3.65 \pm 0.57 \text{ Tg}$	$2.08 \pm 0.47 \text{ Tg}$
$HLFREM_{AG} \\$	$28.67 \pm 7.04 \ Tg$	$18.30\pm3.76\ Tg$	$2.96 \pm 0.47 \ Tg$	$1.69 \pm 0.38 \; Tg$
FEER	$56.95 \pm 13.99 \text{ Tg}$	$31.49 \pm 6.46 \ Tg$	$10.48\pm1.65\ Tg$	$3.00 \pm 0.67 \ Tg$
GFAS v1.2	$50.72 \pm 12.04 \ Tg$	$32.14 \pm 6.38 \; Tg$	$14.02\pm2.49\ Tg$	$3.52\pm0.74\ Tg$
GFED v4.1s	$49.60 \pm 14.82 \ Tg$	$31.40\pm7.96\ Tg$	$7.57 \pm 1.13 \; Tg$	$2.47 \pm 0.57 \ Tg$





#### 5. Summary and Conclusions

Taking advantage of the increased number of polar orbiting satellite overpasses nearer the poles, we have extended the Fire Radiative Energy Emissions (FREM) approach to direct "top down" fire emissions estimation to High Latitudes (HL) fires, and to polar-orbiting FRP datasets. Previously the approach was limited to use on low-to-mid latitude geostationary FRP data (Nguyen et al., 2023). This highly direct approach to estimating fire emissions uses only satellite observations of fire radiative power and CO, removing the need for assuming the amount of biomass per unit area, pre-fire fuel loads and combustion completeness, or correlations between FRE and burned biomass developed in the laboratory, in small scale fires, or elsewhere. Negating the requirements for these parameters removes a key source of uncertainty associated with other emissions estimation techniques (Kasischke and Penner, 2004; Reid et al., 2009; Wooster et al., 2015), and provides a means of converting the FRE data from the Global Fire Assimilation system (GFAS) into fire emissions without use of factors derived via linear regressions against the GFED burned biomass totals, as is used currently within GFAS (Kaiser et al., 2012).

Via a set of 708 matchup fires across four regions of interest in the HL region above  $60^{\circ}$ N, we used S5P TROPMI Total Column Carbon Monoxide (TCCO) data to calculate total plume CO and total FRE up to the time of the S5P overpass from GFAS v1.4. From these data a set of biome specific CO emission coefficients ( $EC_{CO}^b$ ) were generated using the approach of (Nguyen et al., 2023) that can then be used to convert further FRP data of fires in the four dominant HL biomes (Deciduous Needleleaf Forests, Evergreen Needleleaf Forests, Grasslands, and Shrublands) to emission rates of CO. Application of these emissions coefficients to the daily FRE totals from GFAS v1.2 enabled us to produce new CO emissions inventory for these four biomes in the HL region, unreliant on any additional parameters or datasets.

The CO emissions derived from this new approach were compared to three other widely used fire emission inventories, those produced and outputted by GFAS v1.2 itself, those from FEERv1.0-GFASv1.2 (calculated using GFAS FRE and a FEER-equivalent  $EC_{CO}^b$ ; (Nguyen et al., 2023)), and those from GFED v4.1s. Total carbon emissions estimates were also calculated based on emission factor ratios between CO and Carbon. The HLFREM CO and Carbon emissions timeseries and CO spatial patterns derived using the HLFREM approach were found to be in good temporal and spatial agreement with the FEER-equivalent, GFAS v1.2, and GFED v4.1s inventories, particularly for the two forested biomes and shrublands, producing relatively similar but generally smaller emissions totals. Mean annual HLFREM CO and carbon emission totals were found to be 28-43% smaller than totals produced by FEER, GFAS v1.2, and GFAS v4.1s for the two forested biomes and Shrubland biomes. HLFREM CO and carbon emission totals from Grassland were also in good temporal and spatial agreement with the other inventories, although the emissions were significantly lower (61-80%) than those from other inventories; and whilst this could be correct, it is also possibly a result of the relatively small number of fire-matchups found during the generation of the HLFREM  $EC_{CO}^{Grassland}$  and perhaps a low bias. Compounding this, the largest difference (GFAS v1.2, 80% lower CO emissions, 74% lower carbon emissions) was found over the Grassland biomes, which in certain of the other databases has some consideration of peat burning included that is not accounted for in the HLFREM methodology. On the other hand, if the matchup fires included areas having peat burning, the impact of this would already be in the derived emissions coefficients/





Future developments in advancing the HLFREM approach will include consideration of this organic soil burning, as well as expansion of both the biomes covered and the number of fire matchups in each. Our aim is to develop a long-term and geographically continuous HL fire emissions dataset that does not rely on parameters taken from modelling, from correlations between inventories, or from conversion coefficients taken from laboratory or small-scale fire experiments when converting the satellite observations into emissions estimates. Instead, the FREM approach uses information extracted from the satellite data itself to generate the necessary conversion coefficients, an approach that we feel has great potential to expand further as both active fire and trace gas remotely sensed datasets continue to advance.

# Appendix A

# Table A1: Aggregated CCI landcover classes (taken from ESA 2017) assigned to each HLFREM biome.

HLFREM Biome (≥60°N)	Full Biome Name	Assigned CCI Class Codes
Managed	Managed	10, 11, 12, 20, 30, 40
EGBroad	Evergreen Broadleaf Forests	50, 160, 170
DecBroad	Deciduous Broadleaf Forests	60, 61, 62, 90
EGNeedle	Evergreen Needleleaf Forests	70, 71, 72
DecNeedle	Deciduous Needleleaf Forests	80, 81, 82
Grassland	Grassland	100, 110, 130, 180, 190
Shrubland	Shrubland	120, 121, 122
Sparce	Sparce	140, 150, 151, 152, 153
Bare	Bare	200, 201, 202
Snow/Ice	Snow and Ice	220

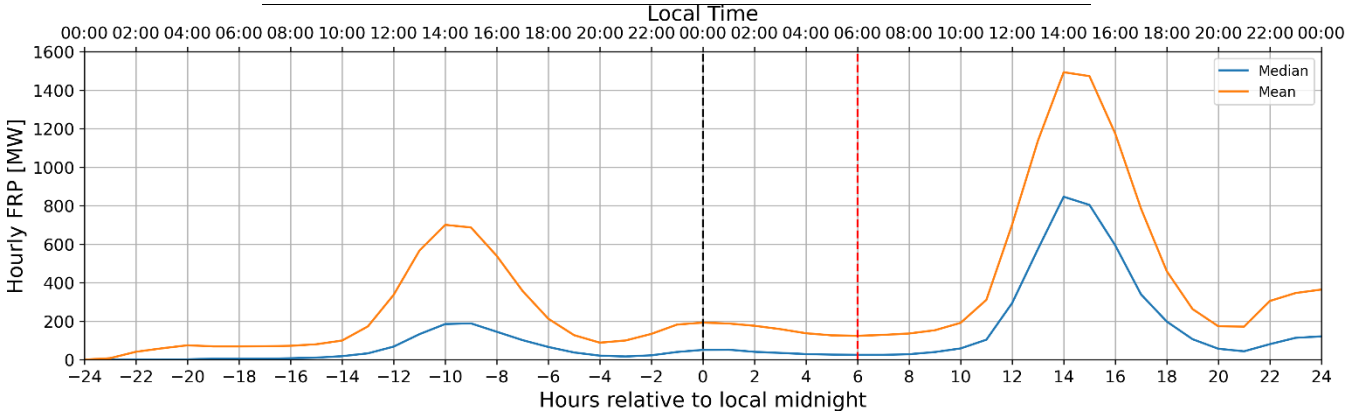


Figure A1: Median (blue) and mean (orange) hourly FRP of all plumes identified in the HLFREM study, during the day before observation (negative hours relative to local midnight) and day of observation (positive hours relative to local midnight) from the hourly FRP dataset. Local midnight and 06:00 local time is shown with the black and red line, respectively.



410

411 412



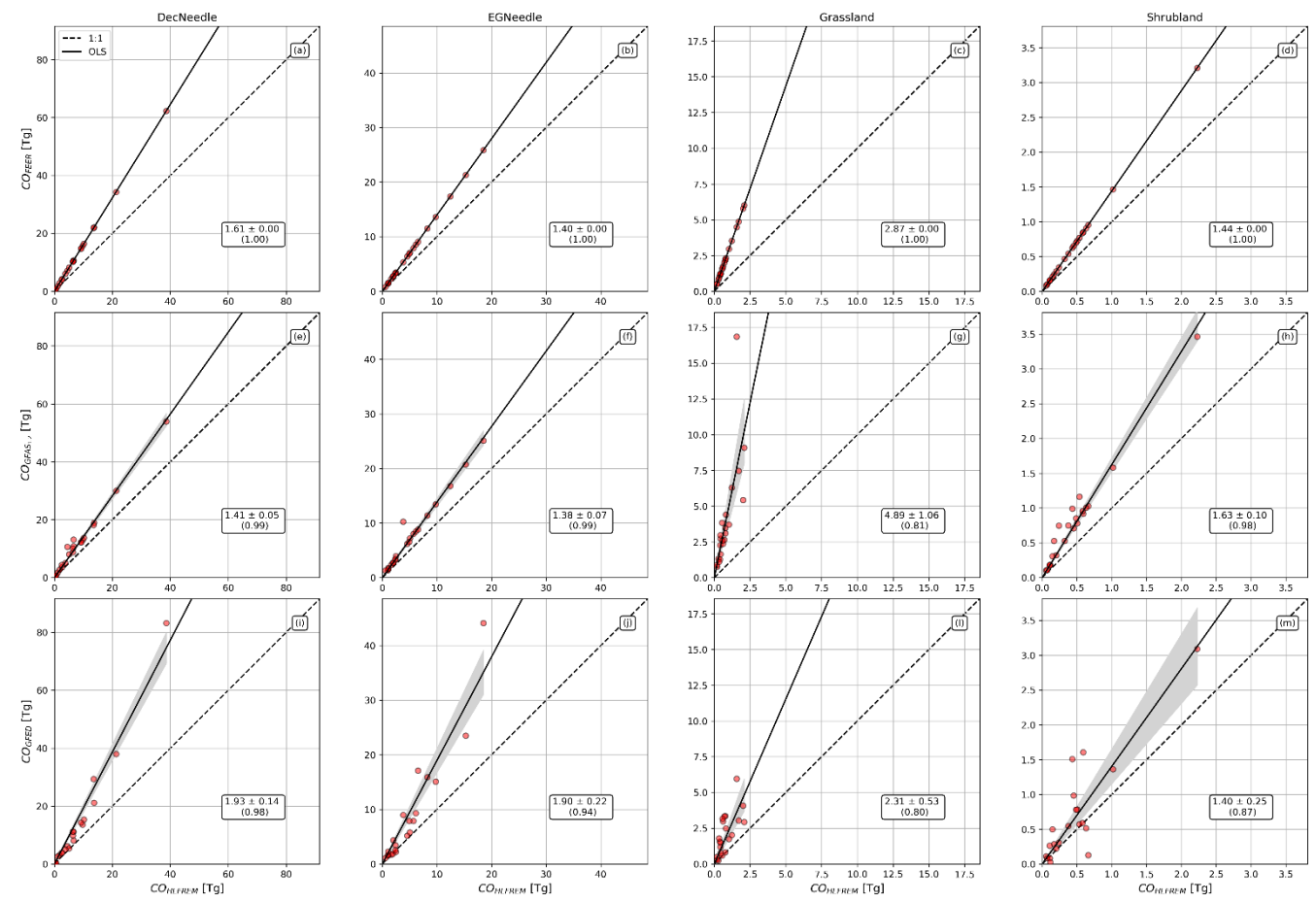


Figure A2: OLS Regression analysis of the Annual HL CO Emissions, comparing the HLFREM emissions (calculated using GFAS v1.2 FRE totals) with (a-d) FEER, (e-h) GFAS v1.2, and (i-l) for Deciduous Needleleaf Forests (a,e,i), Evergreen Needleleaf Forests (b,f,j), Grassland (c,g,k), and Shrubland (d,h,l) biomes. OLS regression and associated errors are shown on each plot (displayed as the solid line and shading respectively), with the R<sup>2</sup> value being shown in the brackets. A 1:1 line (dashed line) is also shown.





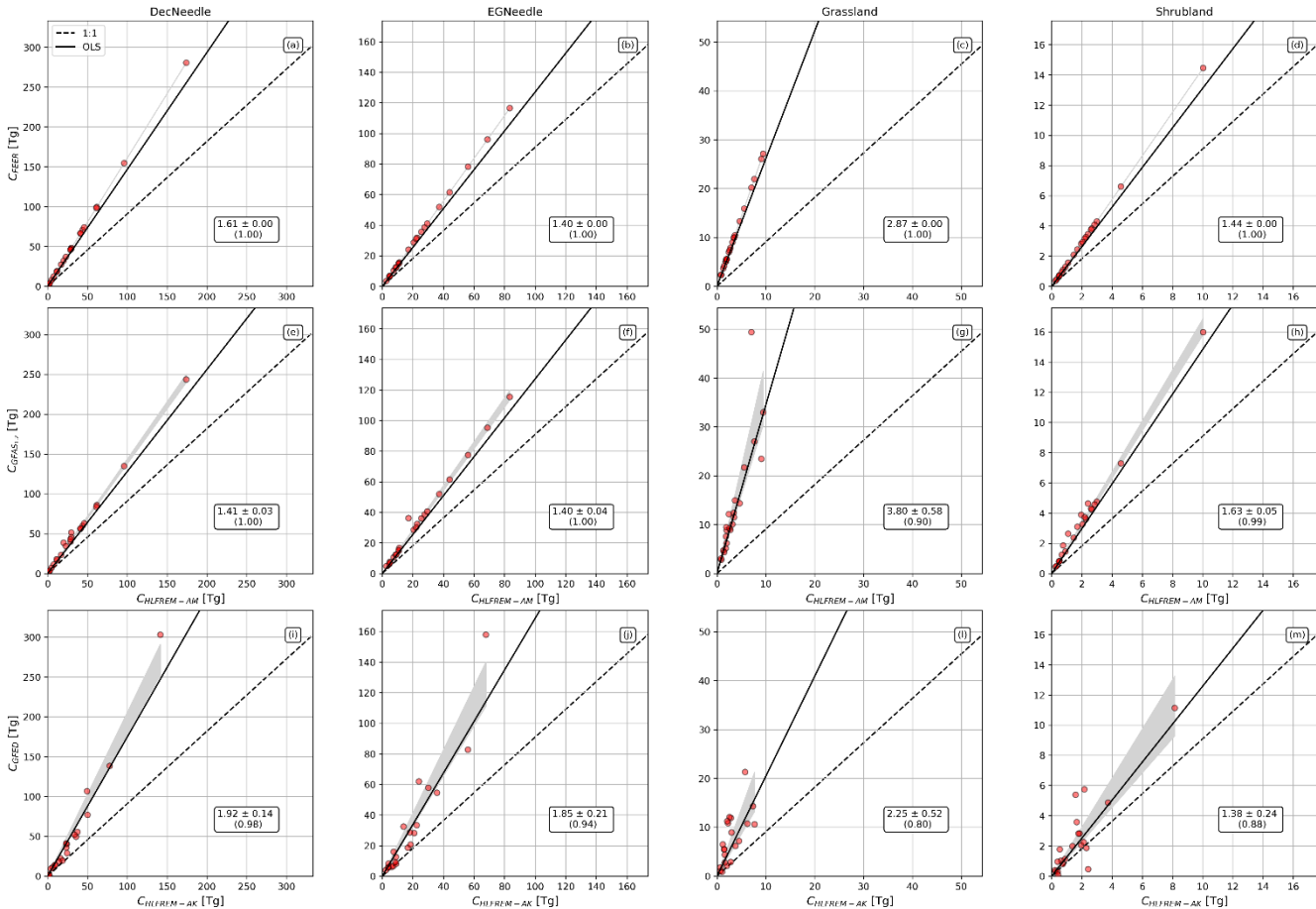


Figure A3: OLS Regression analysis of the Annual HL C Emissions, comparing the HLFREM emissions (calculated using GFAS v1.2 FRE totals) with (a-d) FEER, (e-h) GFAS v1.2, and (i-l) for Deciduous Needleleaf Forests (a,e,i), Evergreen Needleleaf Forests (b,f,j), Grassland (c,g,k), and Shrubland (d,h,l) biomes. As the HLFREM C Emissions have been calculated via EF ratios with respect to Carbon Monoxide, different EF ratios have been used to compare FEER and GFAS v1.2 (using EFs from (Andreae and Merlet, 2001), referred to as HLFREMAM), and GFEDv4.1s (using EFs from (Akagi et al., 2011), referred to as HLFREMAG). OLS regression and associated errors are shown on each plot (displayed as the solid line and shading respectively), with the R<sup>2</sup> value being shown in the brackets. A 1:1 line (dashed line) is also shown.

## 7. Code Availability

422 Code is available upon request to William Maslanka (william.maslanka@kcl.ac.uk).

### 8. Data Availability

Sentinel-5P products are distributed freely by the Copernicus Data Space Ecosystem (https://dataspace.copernicus.eu/, last accessed 19 March 2025), as is the VIIRS and MODIS AF and Multispectral Products by the LAADS DAAC (https://ladsweb.modaps.eosdis.nasa.gov/, last accessed 19 March 2025), and the VIIRS AOD EPS product on the NOAA





- 427 Comprehensive Large Array-Data Stewardship System (CLASS, https://www.aev.class.noaa.gov/, last accessed 19 March
- 428 2025). GFAS v1.2 data is distributed freely through the ECMWF Atmosphere Data Store
- 429 (https://ads.atmosphere.copernicus.eu/, last accessed 19 March 2025). GFAS v1.4 data used in this study is available upon
- 430 request. GFED v4.1s data is distributed freely from the GFED web portal (https://www.globalfiredata.org/, last accessed 19
- 431 March 2025). FEER data is distributed freely on the Fire Energetics and Emission Research website
- 432 (https://feer.gsfc.nasa.gov/index.php, last accessed on 19 March 2025).

#### 433 9. Author Contributions

- 434 W.M.: Conceptualization, Data curation, Formal analysis, Investigation, Methodology, Project administration, Software,
- 435 Validation, Visualization, Writing original draft, and Writing review & editing.
- 436 M.W.: Conceptualization, Formal analysis, Funding acquisition, Methodology, Supervision, Writing original draft, and
- 437 Writing review & editing.
- 438 Z.L.: Data curation, Resources, Software, and Writing review & editing.
- 439 J.H.: Resources, Software, and Writing review & editing.

#### 440 10. Competing Interests

441 The authors declare that they have no conflict of interest.

# 442 11. Acknowledgements

- 443 Neither the European Commission nor ECMWF is responsible for any use that may be made of the information it contains.
- 444 The authors would like to thank Mark Parrington and Enza Di Tomaso of the ECMWF for the provision of GFAS v1.4 data,
- as well as members of the KCL Wildfire and Earth Observation research group, who have helped to improve the quality and
- 446 content of the research and of this paper.

# 447 12. Financial Support

- 448 This work was supported by the Natural Environment Research Council (NERC) National Centre for Earth Observation
- 449 (NCEO) funding under grants NE/R016518/1 and NE/Y006216/1. This research is also an output of the Leverhulme Centre
- 450 for Wildfires, Environment and Society through the Leverhulme Trust, grant number RC-2018-023.





#### 451 References

- 452 Akagi, S. K., Yokelson, R. J., Wiedinmyer, C., Alvarado, M. J., Reid, J. S., Karl, T., Crounse, J. D., and Wennberg, P. O.:
- 453 Emission factors for open and domestic biomass burning for use in atmospheric models, Atmos Chem Phys, 11, 4039–4072,
- 454 https://doi.org/10.5194/acp-11-4039-2011, 2011.
- 455 Andela, N., Kaiser, J. W., van der Werf, G. R., and Wooster, M. J.: New fire diurnal cycle characterizations to improve fire
- 456 radiative energy assessments made from MODIS observations, Atmos Chem Phys, 15, 8831-8846,
- 457 https://doi.org/10.5194/acp-15-8831-2015, 2015.
- 458 Andreae, M. O.: Emission of trace gases and aerosols from biomass burning an updated assessment, Atmos Chem Phys, 19,
- 459 8523–8546, https://doi.org/10.5194/acp-19-8523-2019, 2019.
- 460 Andreae, M. O. and Merlet, P.: Emission of trace gases and aerosols from biomass burning, Global Biogeochem Cycles, 15,
- 461 955–966, https://doi.org/10.1029/2000GB001382, 2001.
- 462 Byrne, B., Liu, J., Bowman, K. W., Pascolini-Campbell, M., Chatterjee, A., Pandey, S., Miyazaki, K., van der Werf, G. R.,
- 463 Wunch, D., Wennberg, P. O., Roehl, C. M., and Sinha, S.: Carbon emissions from the 2023 Canadian wildfires, Nature, 633,
- 464 835–839, https://doi.org/10.1038/s41586-024-07878-z, 2024.
- Chen, Y., Hall, J., van Wees, D., Andela, N., Hantson, S., Giglio, L., van der Werf, G. R., Morton, D. C., and Randerson, J.
- 466 T.: Multi-decadal trends and variability in burned area from the fifth version of the Global Fire Emissions Database (GFED5),
- 467 Earth Syst Sci Data, 15, 5227–5259, https://doi.org/10.5194/essd-15-5227-2023, 2023.
- 468 Crutzen, P. J. and Andreae, M. O.: Biomass Burning in the Tropics: Impact on Atmospheric Chemistry and Biogeochemical
- 469 Cycles, Science (1979), 250, 1669–1678, 1990.
- 470 Darmenov, A. and da Silva, A.: The quick fire emissions dataset (OFED) Documentation of versions 2.1, 2.2 and 2.4.
- 471 NASA//TM-2015-104606, Greenbelt, MD 20771, 1–212 pp., 2015.
- 472 Davidson, E. A. and Janssens, I. A.: Temperature sensitivity of soil carbon decomposition and feedbacks to climate change,
- 473 Nature, 440, 165–173, https://doi.org/10.1038/nature04514, 2006.
- 474 Dodd, W., Scott, P., Howard, C., Scott, C., Rose, C., Cunsolo, A., and Orbinski, J.: Lived experience of a record wildfire
- 475 season in the Northwest Territories, Canada, Canadian Journal of Public Health, 109, 327-337.
- 476 https://doi.org/10.17269/s41997-018-0070-5, 2018.
- 477 ESA: Land Cover CCI Product User Guide Version 2. Tech. Rep., 2017.
- 478 Fisher, D., Wooster, M. J., Xu, W., Thomas, G., and Lestari, P.: Top-down estimation of particulate matter emissions from
- 479 extreme tropical peatland fires using geostationary satellite fire radiative power observations, Sensors (Switzerland), 20, 1–
- 480 25, https://doi.org/10.3390/s20247075, 2020.
- 481 Freeborn, P. H., Wooster, M. J., Hao, W. M., Ryan, C. A., Nordgren, B. L., Baker, S. P., and Ichoku, C.: Relationships between
- 482 energy release, fuel mass loss, and trace gas and aerosol emissions during laboratory biomass fires, Journal of Geophysical
- 483 Research: Atmospheres, 113, https://doi.org/10.1029/2007JD008679, 2008.





- 484 Friedlingstein, P., Lovenduski, N., Lewis, S., Schuur, E., Turetsky, M., and Smith, A.: Climate change weakens carbon sinks
- 485 and further amplifies climate change, Critical Issues in Climate Change Science, 1-4,
- 486 https://doi.org/https://doi.org/10.5281/zenodo.5596739., 2021.
- 487 Giglio, L., Randerson, J. T., and van der Werf, G. R.: Analysis of daily, monthly, and annual burned area using the fourth-
- 488 generation global fire emissions database (GFED4), J Geophys Res Biogeosci, 118, 317-328,
- 489 https://doi.org/10.1002/jgrg.20042, 2013.
- 490 Giglio, L., Schroeder, W., and Justice, C. O.: The collection 6 MODIS active fire detection algorithm and fire products, Remote
- 491 Sens Environ, 178, 31–41, https://doi.org/10.1016/j.rse.2016.02.054, 2016.
- 492 Di Giuseppe, F., Rémy, S., Pappenberger, F., and Wetterhall, F.: Using the Fire Weather Index (FWI) to improve the estimation
- 493 of fire emissions from fire radiative power (FRP) observations, Atmos Chem Phys, 18, 5359-5370
- 494 https://doi.org/10.5194/acp-18-5359-2018, 2018.
- Hodges, J. A., Price, J. N., Nicotra, A. B., Neeman, T., and Guja, L. K.: Smoke and heat accelerate and increase germination
- 496 in fire-prone temperate grassy ecosystems, Ecosphere, 12, https://doi.org/10.1002/ecs2.3851, 2021.
- 497 Hutto, R. L.: The Ecological Importance of Severe Wildfires: Some Like It Hot, Ecological Applications, 18, 1827–1834,
- 498 https://doi.org/10.1890/08-0895.1, 2008.
- 499 Ichoku, C. and Ellison, L.: Global top-down smoke-aerosol emissions estimation using satellite fire radiative power
- 500 measurements, Atmos Chem Phys, 14, 6643–6667, https://doi.org/10.5194/acp-14-6643-2014, 2014.
- 501 Inness, A., Ades, M., Agustí-Panareda, A., Barré, J., Benedictow, A., Blechschmidt, A.-M., Dominguez, J. J., Engelen, R.,
- 502 Eskes, H., Flemming, J., Huijnen, V., Jones, L., Kipling, Z., Massart, S., Parrington, M., Peuch, V.-H., Razinger, M., Remy,
- 503 S., Schulz, M., and Suttie, M.: The CAMS reanalysis of atmospheric composition, Atmos Chem Phys, 19, 3515-3556,
- 504 https://doi.org/10.5194/acp-19-3515-2019, 2019.
- Jones, M. W., Abatzoglou, J. T., Veraverbeke, S., Andela, N., Lasslop, G., Forkel, M., Smith, A. J. P., Burton, C., Betts, R.
- 506 A., van der Werf, G. R., Sitch, S., Canadell, J. G., Santín, C., Kolden, C., Doerr, S. H., and Le Quéré, C.: Global and Regional
- 507 Trends and Drivers of Fire Under Climate Change, Reviews of Geophysics, 60, https://doi.org/10.1029/2020RG000726, 2022.
- 508 Kaiser, J. W., Heil, A., Andreae, M. O., Benedetti, A., Chubarova, N., Jones, L., Morcrette, J. J., Razinger, M., Schultz, M.
- 509 G., Suttie, M., and Van Der Werf, G. R.: Biomass burning emissions estimated with a global fire assimilation system based on
- observed fire radiative power, https://doi.org/10.5194/bg-9-527-2012, 2012.
- Kaiser, K., Parrington, M., and Armenteras, D.: Biomass Burning in "State of the Climate 2023," Bull Am Meteorol Soc, 105,
- 512 S107–S109, https://doi.org/10.1175/BAMS-D-24-0116.1, 2024.
- 513 Kasischke, E. S. and Penner, J. E.: Improving global estimates of atmospheric emissions from biomass burning, Journal of
- 514 Geophysical Research: Atmospheres, 109, https://doi.org/10.1029/2004JD004972, 2004.
- 515 Kharuk, V. I., Ponomarev, E. I., Ivanova, G. A., Dvinskaya, M. L., Coogan, S. C. P., and Flannigan, M. D.: Wildfires in the
- 516 Siberian taiga, Ambio, 50, 1953–1974, https://doi.org/10.1007/s13280-020-01490-x, 2021.





- 517 Liu, Z., Eden, J. M., Dieppois, B., Drobyshev, I., Gallo, C., and Blackett, M.: Were Meteorological Conditions Related to the
- 518 2020 Siberia Wildfires Made More Likely by Anthropogenic Climate Change?, Bull Am Meteorol Soc, 103, S44-S49,
- 519 https://doi.org/10.1175/BAMS-D-21-0168.1, 2022.
- 520 Masrur, A., Petrov, A. N., and DeGroote, J.: Circumpolar spatio-temporal patterns and contributing climatic factors of wildfire
- 521 activity in the Arctic tundra from 2001-2015, https://doi.org/10.1088/1748-9326/aa9a76, 1 January 2018.
- 522 McCarty, J. L., Aalto, J., Paunu, V. V., Arnold, S. R., Eckhardt, S., Klimont, Z., Fain, J. J., Evangeliou, N., Venäläinen, A.,
- 523 Tchebakova, N. M., Parfenova, E. I., Kupiainen, K., Soja, A. J., Huang, L., and Wilson, S.: Reviews and syntheses: Arctic fire
- 524 regimes and emissions in the 21st century, https://doi.org/10.5194/bg-18-5053-2021, 15 September 2021.
- 525 Mekonnen, Z. A., Riley, W. J., Randerson, J. T., Shirley, I. A., Bouskill, N. J., and Grant, R. F.: Wildfire exacerbates high-
- 526 latitude soil carbon losses from climate warming, Environmental Research Letters, 17, 094037, https://doi.org/10.1088/1748-
- 527 9326/ac8be6, 2022.
- 528 Mota, B. and Wooster, M. J.: A new top-down approach for directly estimating biomass burning emissions and fuel
- 529 consumption rates and totals from geostationary satellite fire radiative power (FRP), Remote Sens Environ, 206, 45–62,
- 530 https://doi.org/10.1016/j.rse.2017.12.016, 2018.
- 531 Nguyen, H. M. and Wooster, M. J.: Advances in the estimation of high Spatio-temporal resolution pan-African top-down
- 532 biomass burning emissions made using geostationary fire radiative power (FRP) and MAIAC aerosol optical depth (AOD)
- 533 data, Remote Sens Environ, 248, https://doi.org/10.1016/j.rse.2020.111971, 2020.
- 534 Nguyen, H. M., He, J., and Wooster, M. J.: Biomass burning CO, PM and fuel consumption per unit burned area estimates
- derived across Africa using geostationary SEVIRI fire radiative power and Sentinel-5P CO data, Atmos Chem Phys, 23, 2089–
- 536 2118, https://doi.org/10.5194/acp-23-2089-2023, 2023.
- 537 NOAA: Visible Infrared Imaging Radiometer Suite (VIIRS) Enterprise Aerosol Optical Depth and Aerosol Particle Size
- 538 Products User's Guide. Version 1, 2020.
- 539 Ponomarev, E., Yakimov, N., Ponomareva, T., Yakubailik, O., and Conard, S. G.: Current Trend of Carbon Emissions from
- 540 Wildfires in Siberia, Atmosphere (Basel), 12, 559, https://doi.org/10.3390/atmos12050559, 2021.
- 541 Popovicheva, O. B., Evangeliou, N., Kobelev, V. O., Chichaeva, M. A., Eleftheriadis, K., Gregorič, A., and Kasimov, N. S.:
- 542 Siberian Arctic black carbon: gas flaring and wildfire impact, Atmos Chem Phys, 22, 5983–6000, https://doi.org/10.5194/acp-
- 543 22-5983-2022, 2022.
- Ramo, R., Roteta, E., Bistinas, I., van Wees, D., Bastarrika, A., Chuvieco, E., and van der Werf, G. R.: African burned area
- 545 and fire carbon emissions are strongly impacted by small fires undetected by coarse resolution satellite data, Proceedings of
- 546 the National Academy of Sciences, 118, https://doi.org/10.1073/pnas.2011160118, 2021.
- 547 Randerson, J. T., Van Der Werf, G. R., Giglio, L., Collatz, G. J., and Kasibhatla, P. S.: Global Fire Emissions Database,
- 548 Version 4.1 (GFEDv4), https://doi.org/10.3334/ORNLDAAC/1293, 2017.
- 549 Reid, J. S., Hyer, E. J., Prins, E. M., Westphal, D. L., Zhang, J., Wang, J., Christopher, S. A., Curtis, C. A., Schmidt, C. C.,
- 550 Eleuterio, D. P., Richardson, K. A., and Hoffman, J. P.: Global Monitoring and Forecasting of Biomass-Burning Smoke:





- 551 Description of and Lessons From the Fire Locating and Modeling of Burning Emissions (FLAMBE) Program, IEEE J Sel Top
- 552 Appl Earth Obs Remote Sens, 2, 144–162, https://doi.org/10.1109/JSTARS.2009.2027443, 2009.
- 553 Roberts, G., Wooster, M. J., Perry, G. L. W., Drake, N., Rebelo, L.-M., and Dipotso, F.: Retrieval of biomass combustion
- 554 rates and totals from fire radiative power observations: Application to southern Africa using geostationary SEVIRI imagery,
- 555 Journal of Geophysical Research: Atmospheres, 110, https://doi.org/10.1029/2005JD006018, 2005.
- 556 Rogers, B. M., Soja, A. J., Goulden, M. L., and Randerson, J. T.: Influence of tree species on continental differences in boreal
- 557 fires and climate feedbacks, Nat Geosci, 8, 228–234, https://doi.org/10.1038/ngeo2352, 2015.
- 558 Schroeder, W., Oliva, P., Giglio, L., and Csiszar, I. A.: The New VIIRS 375 m active fire detection data product: Algorithm
- description and initial assessment, Remote Sens Environ, 143, 85–96, https://doi.org/10.1016/j.rse.2013.12.008, 2014.
- 560 Turetsky, M., Wieder, K., Halsey, L., and Vitt, D.: Current disturbance and the diminishing peatland carbon sink, Geophys
- 561 Res Lett, 29, https://doi.org/10.1029/2001GL014000, 2002.
- 562 Warneke, C., Schwarz, J. P., Dibb, J., Kalashnikova, O., Frost, G., Al-Saad, J., Brown, S. S., Brewer, Wm. A., Soja, A., Seidel,
- 563 F. C., Washenfelder, R. A., Wiggins, E. B., Moore, R. H., Anderson, B. E., Jordan, C., Yacovitch, T. I., Herndon, S. C., Liu,
- 564 S., Kuwayama, T., Jaffe, D., Johnston, N., Selimovic, V., Yokelson, R., Giles, D. M., Holben, B. N., Goloub, P., Popovici, I.,
- Trainer, M., Kumar, A., Pierce, R. B., Fahey, D., Roberts, J., Gargulinski, E. M., Peterson, D. A., Ye, X., Thapa, L. H., Saide,
- P. E., Fite, C. H., Holmes, C. D., Wang, S., Coggon, M. M., Decker, Z. C. J., Stockwell, C. E., Xu, L., Gkatzelis, G., Aikin,
- 567 K., Lefer, B., Kaspari, J., Griffin, D., Zeng, L., Weber, R., Hastings, M., Chai, J., Wolfe, G. M., Hanisco, T. F., Liao, J.,
- 568 Campuzano Jost, P., Guo, H., Jimenez, J. L., and Crawford, J.: Fire Influence on Regional to Global Environments and Air
- 569 Quality (FIREX-AQ), Journal of Geophysical Research: Atmospheres, 128, https://doi.org/10.1029/2022JD037758, 2023.
- van der Werf, G. R., Randerson, J. T., Giglio, L., Collatz, G. J., Mu, M., Kasibhatla, P. S., Morton, D. C., DeFries, R. S., Jin,
- 571 Y., and van Leeuwen, T. T.: Global fire emissions and the contribution of deforestation, savanna, forest, agricultural, and peat
- 572 fires (1997–2009), Atmos Chem Phys, 10, 11707–11735, https://doi.org/10.5194/acp-10-11707-2010, 2010.
- van der Werf, G. R., Randerson, J. T., Giglio, L., van Leeuwen, T. T., Chen, Y., Rogers, B. M., Mu, M., van Marle, M. J. E.,
- 574 Morton, D. C., Collatz, G. J., Yokelson, R. J., and Kasibhatla, P. S.: Global fire emissions estimates during 1997–2016, Earth
- 575 Syst Sci Data, 9, 697–720, https://doi.org/10.5194/essd-9-697-2017, 2017.
- 576 Wiedinmyer, C., Akagi, S. K., Yokelson, R. J., Emmons, L. K., Al-Saadi, J. A., Orlando, J. J., and Soja, A. J.: The Fire
- 577 INventory from NCAR (FINN): a high resolution global model to estimate the emissions from open burning, Geosci Model
- 578 Dev, 4, 625–641, https://doi.org/10.5194/gmd-4-625-2011, 2011.
- 579 Wooster, M. J. and Zhang, Y. H.: Boreal forest fires burn less intensely in Russia than in North America, Geophys Res Lett,
- 580 31, https://doi.org/10.1029/2004GL020805, 2004.
- 581 Wooster, M. J., Roberts, G., Perry, G. L. W., and Kaufman, Y. J.: Retrieval of biomass combustion rates and totals from fire
- 582 radiative power observations: FRP derivation and calibration relationships between biomass consumption and fire radiative
- 583 energy release, Journal of Geophysical Research Atmospheres, 110, 1–24, https://doi.org/10.1029/2005JD006318, 2005.





- Wooster, M. J., Xu, W., and Nightingale, T.: Sentinel-3 SLSTR active fire detection and FRP product: Pre-launch algorithm
- 585 development and performance evaluation using MODIS and ASTER datasets, Remote Sens Environ, 120, 236-254,
- 586 https://doi.org/10.1016/j.rse.2011.09.033, 2012.
- 587 Wooster, M. J., Roberts, G., Freeborn, P. H., Xu, W., Govaerts, Y., Beeby, R., He, J., Lattanzio, A., Fisher, D., and Mullen,
- 588 R.: LSA SAF Meteosat FRP products Part 1: Algorithms, product contents, and analysis, Atmos Chem Phys, 15, 13217–
- 589 13239, https://doi.org/10.5194/acp-15-13217-2015, 2015.
- 590 Wooster, M. J., Roberts, G. J., Giglio, L., Roy, D., Freeborn, P., Boschetti, L., Justice, C., Ichoku, C., Schroeder, W., Davies,
- 591 D., Smith, A., Setzer, A., Csiszar, I., Strydom, T., Frost, P., Zhang, T., Xu, W., de Jong, M., Johnston, J., Ellison, L., Vadrevu,
- 592 K., McCarty, J., Tanpipat, V., Schmidt, C., and San-Miguel, J.: Satellite remote sensing of active fires: History and current
- status, applications and future requirements, https://doi.org/10.1016/j.rse.2021.112694, 15 December 2021.
- 594 Xu, W., Wooster, M. J., Roberts, G., and Freeborn, P.: New GOES imager algorithms for cloud and active fire detection and
- 595 fire radiative power assessment across North, South and Central America, Remote Sens Environ, 114, 1876-1895,
- 596 https://doi.org/10.1016/j.rse.2010.03.012, 2010.
- 597 Xu, W., Wooster, M. J., Kaneko, T., He, J., Zhang, T., and Fisher, D.: Major advances in geostationary fire radiative power
- 598 (FRP) retrieval over Asia and Australia stemming from use of Himarawi-8 AHI, Remote Sens Environ, 193, 138-149,
- 599 https://doi.org/10.1016/j.rse.2017.02.024, 2017.
- 600 Xu, W., Wooster, M. J., He, J., and Zhang, T.: First study of Sentinel-3 SLSTR active fire detection and FRP retrieval: Night-
- 601 time algorithm enhancements and global intercomparison to MODIS and VIIRS AF products, Remote Sens Environ, 248,
- 602 111947, https://doi.org/10.1016/j.rse.2020.111947, 2020.
- 603 Xu, W., Wooster, M. J., He, J., and Zhang, T.: Improvements in high-temporal resolution active fire detection and FRP retrieval
- 604 over the Americas using GOES-16 ABI with the geostationary Fire Thermal Anomaly (FTA) algorithm, Science of Remote
- 605 Sensing, 3, 100016, https://doi.org/10.1016/j.srs.2021.100016, 2021.

606